Accepted to Phys. Fluids 10.1063/5.0156111

Investigating the Aerodynamic Drag and Noise Characteristics of a Standard Squareback Vehicle with Inclined Side-View Mirror configurations using a Hybrid Computational Aeroacoustics (CAA) Approach

K. K. Chode [a], H. Viswanathan [a, b *], K. Chow [c], H. Reese [d]

[a] Materials and Engineering Research Institute, Sheffield Hallam University, Howard Street, Sheffield, England, S1 1WB, United Kingdom.

[b] Department of Engineering and Mathematics, Sheffield Hallam University, Howard Street, Sheffield, England, S1 1WB, United Kingdom

[c] HORIBA MIRA Ltd., Watling Street, Nuneaton Warwickshire, CV10 0TU, United Kingdom.

[d] ANSYS Germany GmbH, Birkenweg 14a, 64925 Darmstadt, Germany.

ABSTRACT

This study investigates the aerodynamic noise generated and radiated from a standard squareback body with various inclined side-view mirrors using a hybrid computational aeroacoustics (CAA) method based on a Stress-blended Eddy Simulation (SBES) coupled with the Ffowcs-Williams and Hawkings (FW-H) acoustic analogy. The results indicate that in the absence of the side-view mirror, the idealised A-pillar is identified as the subsequent major contributor to the overall noise radiated from the vehicle body, and the coefficient of drag decreases by approximately 13.3% despite a minimal change in the projected frontal area. However, the behaviour of the drag coefficient becomes nonlinear and highly dependent on the complex flow features, including the vortex shedding patterns and the interaction between the flow and side surface of the body, with increasing mirror inclination angle. In contrast, the radiated noise exhibits a constant decrease as the mirror inclination angle (θ) increases to 32°. Additionally, when the side-view mirror is considered as the sole source, the noise radiated is minimal for an inclination angle of 16°, and a further increase in inclination angle has no significant reduction on the noise radiated but alters the overall drag coefficient of the vehicle. These findings have practical implications for the design of side-view mirrors to reduce aerodynamic noise in automotive applications and highlight the complex trade-offs between noise reduction and changes in the drag coefficient that must be considered in such designs.

* Corresponding author. Email address: h.viswanathan@shu.ac.uk (H. Viswanathan); Phone: +0441142256244.

Accepted to Phys. Fluids 10.1063/5.0156111

NOMENCLATURE

x, y, z	3D Cartesian coordinates (Streamwise, normal, spanwise)
L	Length of the Vehicle
W	Width of the Vehicle
H	Height of the Vehicle
L_c	The characteristic length of the Mirror
U_∞	Freestream velocity
Re_L	Reynolds Number based on Length of the Vehicle
$Cd_{vehicle}$	Drag Coefficient of the whole vehicle
$Cl_{vehicle}$	Lift Coefficient of the whole vehicle
Cp	Pressure coefficient
p'	Pressure fluctuations
St	Strouhal number
F_A	Frontal area
CdA	Area weighted Drag Coefficient
θ	The angle of mirror inclination
V_1, V_2	Mirror induced vorticity
w_m	Side of the vehicle with mirror
w'_m	Side of the vehicle without a mirror
α	The angle between the A-pillar and the flow interaction line
L_{hx}	The thickness of the horseshoe vortex
L_{hy+}	Width of the horseshoe vortex in the positive normal direction
L_{hy-}	Width of the horseshoe vortex in the negative normal direction
L_{hz}	Width of the horseshoe vortex in the normal direction
L_{ws}	Length of the mirror wake
p'_{rms}	Root mean square of hydrodynamic pressure fluctuations
Np'_{rms}	Normalised hydrodynamic pressure fluctuations.
p'_n	Sound pressure
p'_{nrms}	Root mean square of sound pressure

Accepted to Phys. Fluids 10.1063/5.0156111

ACRONYMS

CAA	Computational Aeroacoustics
DDES	Delayed DES
DES	Detached Eddy Simulation
FW-H	Ffowcs-Williams and Hawkings
GIS	Grid Induced Separation
HPF	Hydrodynamic Pressure Fluctuations
IDDES	Improved DDES
KI	Kirchhoff Integral
OASPL	Overall Sound Pressure level
RANS	Reynolds-Averaged Navier Stokes
RMS	Root Mean Square
SBES	Stress-Blended Eddy Simulation
SPL	Sound Pressure Level

Accepted to Phys. Fluids 10.1063/5.0156111

INTRODUCTION

Acoustic comfort has become an integral part of road vehicle development, particularly for passenger vehicles.[1–4] The noise perceived inside and outside a passenger vehicle is a combination of various sources that contribute to overall noise. The noise sources in a vehicle can be classified into at least four categories: a rolling noise source generated by the interaction of the tire with the road[5], a powertrain noise source generated by the engine and powertrain[6], wind-induced noise from the airflow around the vehicle[7], and other noise sources such as sloshing noise resulting from the interaction of liquids with solid surfaces[8,9] and noise sources from vibrations of the vehicle structure.[10] The shift towards *e*-mobility only accentuates the significance of acoustic design because the absence of noise from combustion engines amplifies other noises such as wind-induced noise and tire noise. Wind-induced noise is of primary importance when a vehicle is cruising as the wind-induced noise increases with an increase in the speed of the vehicle and dominates tire noise around 100 km/h.[11–14]

The flow past the side-view mirror is highly turbulent, and the interplay of the turbulent flow from the side-view mirror and A-pillar with the side window is the major contributor to wind-induced noise.[15] The turbulent flow causes pressure fluctuations which result in noise that propagates externally. In addition, when these pressure fluctuations interact with the vehicle surface such as the side window, results in noise generation that transmits to the vehicle cabin and propagates outside. Therefore, the noise generated by a vehicle can be reduced by reducing the intensity of pressure fluctuations, thereby reducing both the external and the internal noise.[4,7] Ideally, these complex interactions are investigated during the design phase using Computational Aeroacoustics (CAA) methods, such as Direct Noise Computation (DNC) and hybrid CAA. When the external noise radiated is considered, hybrid CAA methods are an efficient way to overcome the challenges of disparity of scales between the energy in the flow and the radiated acoustic energy in the CAA method, and reduce the computational effort. The hybrid CAA method is a two-step approach in which the incompressible Navier-Stokes (NS) equation is solved to obtain the hydrodynamic component, that is, the pressure fluctuations from the flow. In the second step, the acoustic pressure fluctuations are obtained by solving an acoustic analogy. Various turbulence modelling approaches based on NS equations can be used to solve the hydrodynamic component in the hybrid CAA method. The most widely used turbulence modelling approaches are based on Reynolds–Averaged Navier Stokes (RANS). Most RANS approaches can predict the force coefficients and large flow features for standard and realistic vehicles.[16–20] However for acoustic predictions, when RANS approaches are

coupled with acoustic analogies, they tend to fall short of predicting both hydrodynamic and acoustic components, as the resolution of flow obtained from this model is not sufficient to accurately predict both hydrodynamic pressure fluctuations exerted on the side window and radiated noise.[21,22] Hybrid RANS-LES methods, such as DES, improve hydrodynamic predictions by partially resolving turbulent flow structures using LES in regions where the flow is dominated by eddies that are mostly non-dissipative in the inertial subrange, whereas RANS in regions of small-scales where the averaging is carried out. Thus, eddies within the inertial subrange are well resolved[17,23] which improves the prediction of fluctuations in flow, thereby improving the input data for acoustic analogies. The resolution of turbulent flow obtained from DES depends on the grid size generated; a smaller grid size improves the resolution, but the grid generated should follow the condition specifically at the walls, where the local grid size should be greater than the boundary layer thickness to avoid grid-induced separation (GIS).[24,25] Large eddy simulations (LES) with denser grid refinements closer to the walls improve both hydrodynamic and acoustic predictions; however, they require tremendous computational resources when applied to complex geometries such as full-scale vehicles. Therefore, to mitigate the GIS and reduce the computational effort, variants of DES simulations have been developed, such as delayed detached eddy simulation (DDES) and improved DDES (IDDES) which are in reasonable agreement with the aerodynamic prediction of complex vehicle shapes.[26,27] However, in some cases, such as a half-round mirror (HRM), staggered cylindrical pins, and back-facing step studies where separated shear layers are involved, the predictions by DDES and IDDES tend to underpredict or over-predict the separation.[28–32] Menter[30] introduced Stress-blended Eddy Simulation (SBES) to overcome the shortcomings of DES and its variants by introducing a strong shielding function which allows a rapid transition from RANS to LES, thereby accurately capturing the flow separation and preventing GIS even for highly refined grids.[2,28,33] Therefore, in this study, SBES is used to obtain hydrodynamic pressure fluctuations over the vehicle.

SAE T4 is widely used for studying aeroacoustics[7,13,14,34–37] owing to the availability of acoustic data from the initial experiments conducted by Islam *et al.*[35] and Hartmann *et al.*[7] The reference body has a front slant and distinctive A-pillar representing an idealised vehicle. An initial study conducted by Islam *et al.*[35] demonstrated the accuracy of numerical methods in predicting sunroof buffeting by comparing predicted and experimental results. They concluded that aerodynamic and acoustic parameters, such as velocity fields and sound pressure level (SPL), were predicted to be in reasonable agreement with experiments using a finite-volume

scheme-based LES model. Hartmann *et al.*[7] used the same body with a modified A-pillar and a realistic side-view mirror geometry to investigate the noise transmission into the passenger cabin through the side window by employing both numerical and experimental techniques. They found that to evaluate the noise transmitted inside the cabin, a compressible simulation must be used, as the acoustic part is the main contributor which can be obtained by implementing a wavenumber-frequency decomposition (WFD) on the pressure fluctuation data obtained by solving the flow equations. In addition, geometric modifications of the side-view mirror geometry, such as enlarging the mirror, were shown to influence the noise level inside the cabin because the WFD results showed strong changes in the acoustic field. Similarly, Dawi and Akkermans[34] conducted a study to recommend an aero-vibro-acoustic methodology based on DNC using a body similar to that of Hartmann *et al.*[7] but with a different realistic mirror geometry. They recommended that the grid generated for aeroacoustics studies should have a smooth transition between two different grid sizes to avoid spurious noise, and proposed an acoustic damping model to further suppress the spurious noise generated by grid interfaces. Similar studies were carried out for SAE T4 without modifying the A-pillar and simplified bluff body as a side-view mirror by Müller *et al.*[37], Becker *et al.*[14], and Nusser and Becker[13] to evaluate the influence of the A-pillar geometry, inflow velocity, and change in mirror cross-section sizes on the overall noise transmitted inside the cabin and to evaluate the most suitable numerical methodology for evaluating the noise transmitted into the cabin. These studies observed that the noise transmitted inside the cabin depends on the flow field and geometry of the forebody before the side window. In addition, they observed that at low frequencies, tonal noise due to periodic fluctuations in the wake of the mirror is only transmitted into the vehicle if the amplitude is high.

The aforementioned studies focused on evaluating and assessing the methodologies for obtaining the noise transmitted inside the cabin, whereas the noise generated and propagated outside the vehicle was not investigated. Stringent regulations were introduced by the European Council (Regulation (EU) No. 540/2014) to reduce the overall noise radiated from passenger vehicles. One of the major sources of noise radiating from electric vehicles is aerodynamically induced noise. To evaluate the noise radiated from a vehicle, techniques such as Ffowcs-Williams and Hawkings (FW-H) are used. FW-H provides a grid-independent solution, where the receiver location can be in the far-field regime. Evaluating radiated noise computationally can also complement expensive noise testing performed experimentally.

The studies conducted by Hartmann *et al.*[7] and Müller *et al.*[37] found that the changes made to either the side-view mirror or the A-pillar have a significant influence on the noise measured away from the vehicle; for example, the change in the cross-section of the mirror increased the noise transmitted inside the cabin and radiated, indicating a fundamental change in the noise source information, such as pressure fluctuations exerted on the modified components. Therefore, investigating the acoustic characteristics of components, such as side-view mirrors, and identifying critical flow features contributing to noise source generation can help understand the noise generation mechanism and propagation. Once the noise source generation is identified, several mitigation approaches can be used by introducing geometrical changes such as varying inclination[2], aspect ratio[2,38], and rounding corners[39]. Ideally, geometrical changes are a way to reduce noise, as opposed to changing the position or replacing it with a new design[40–46], and the changes made to the geometry can influence the aerodynamic performance, such as the drag coefficient of the component and the overall aerodynamic performance of the vehicle. Therefore, it is critical to understand the changes in the overall drag behaviour when geometrical changes are introduced into the component to mitigate noise. In addition, the generated tonal components can be identified by investigating the propagation of noise closer to the side window.

This study is inspired by the lack of understanding regarding the connection between drag and noise for full-scale vehicle bodies when modifications are introduced to mitigate noise through simplified changes in the side-view mirror geometry. The present study has three objectives: *i*) to assess the accuracy of the hybrid CAA method, which uses the SBES turbulence model and FW-H[2], through a full-scale square-back vehicle, that is, the SAE T4 vehicle, by comparing the predicted results with experimental data published by Müller *et al.*[37] and Nusser[47]. *ii*) To assess the contributions of the side-view mirror to both vehicle drag and noise generated. *iii*) To understand the impact of changing the inclination of the mirror on the overall drag and noise generated and radiated from SAE T4.

NUMERICAL METHODOLOGY

A. Geometry description and computational domain

In this study, the geometry of a full-scale SAE reference square-back body, referred to as SAE T4 is used with a standardised mirror geometry representing a square cylinder with a characteristic length ($l_c = 0.08$ m) mounted on one side of the body perpendicular to the surface, as shown in Fig.1(a). The selection of the geometry is based on the availability of reliable and consistent data from previous studies conducted by Nusser[47], Nusser and Becker[13], Becker *et al.*[14] and Müller *et al.*[37] These studies have presented reproducible data using the SAE T4 geometry without modifying any features that are proprietary in nature. The SAE squareback body was mounted on four struts with a height of $y/H = 0.14$. A freestream velocity $U_\infty = 27.78$ m/s, which corresponds to a Reynolds number $Re_L = 7 \times 10^6$ based on the length (L) of the SAE reference body which is identical to the experimental setup used by Nusser[47] and Müller *et al.*[37] Also, the pressure sensor probed on the side window shown in Fig.1(c) is identical to the experimental study.

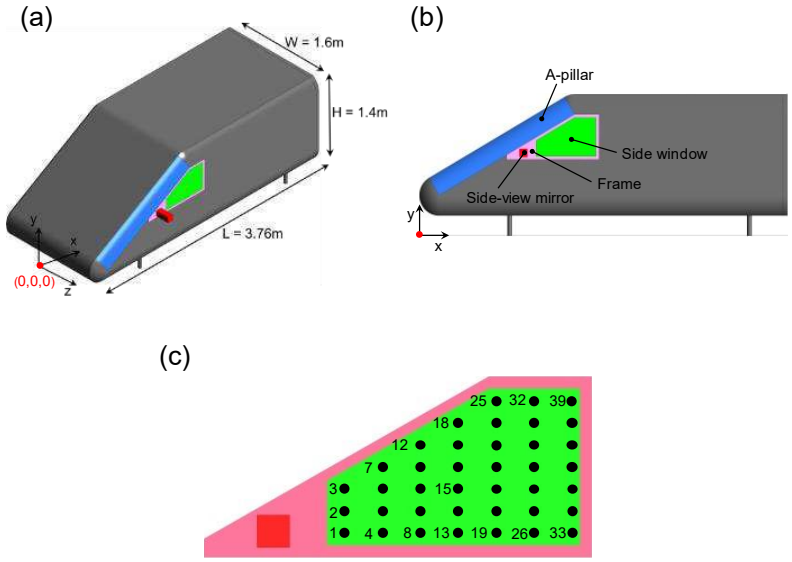

Fig. 1. a) SAE Reference squareback (SAET4) model with a bluff mirror mounted in the positive spanwise direction and a red dot representing the origin; b) naming conventions used for SAE T4 design features; c) schematic representation of surface pressure probe locations on the side window.

The computational domain is 12 L x 3.6 L x 3.6 L, where L represents the length of the vehicle (L = 3.76 m) shown in Fig. 2 and the computational domain is defined based on

ERCOFTAC guidelines adapted from the previous studies conducted.[22,35] The blockage ratio with the domain cross-section was ~ 1.5%. The inlet was located at 3 L from the origin located at the centre of the nose end of SAE T4, and a uniform velocity condition was imposed on the inlet with a turbulent intensity of 0.1%. A constant zero-pressure outlet located at 12 L was applied to the outlet. The walls surrounding the domain in the spanwise and normal directions were set as symmetrical, and a no-slip boundary condition was applied to both SAE T4 and the ground. The walls surrounding the domain in the spanwise and normal directions were set as symmetrical, and a no-slip boundary condition was applied to both the SAE squareback and the ground.

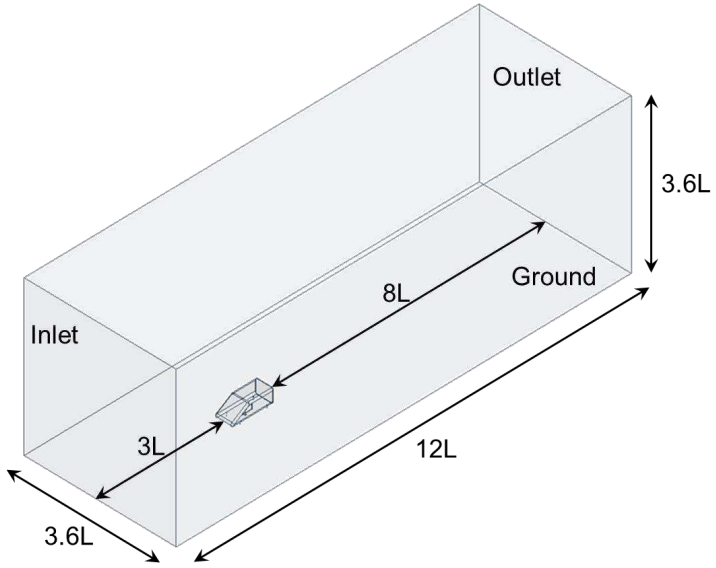

Fig. 2. Overview of computational domain with boundary conditions used in this study.

B. Grid generation

In this study, a poly hex core unstructured grid was used and generated using the ANSYS Mosaic meshing methodology. The Poly-hex core grid contains polyhedral cells on the surface of the domain and body, whereas the core contains hexahedral cells. A transition layer of polyhedral cells was generated to accommodate the transition from boundary layer cells to freestream. Several local refinement zones were generated to ensure that the generated grid had a smooth transition and resolve turbulence to accurately capture flow. For the grid evaluation study, three grids were generated: coarse, medium, and fine grids. The surface sizes used in

this study were determined based on the wall-normalised units and characteristic length scale, similar to the methodology presented in Chode *et al.*[2,32] The wall-normalised unit Δy^+ was ensured to be < 1, while the surface sizes were gradually reduced. The grid sizes used for all the grids are presented in Table I. The wall-normalised units were calculated using Eq. 1. An overview of the grid generated for the medium grid is shown in Fig. 3.

$$\Delta x^+ = \frac{u_x{}^*\Delta x}{v};\ \Delta y^+ = \frac{u_y{}^*\Delta y}{v};\ \Delta z^+ = \frac{u_z{}^*\Delta z}{v} \tag{1}$$

where, $\Delta x^+, \Delta y^+$, and Δz^+ are the wall distance units in x, y and z, respectively; v is the kinematic viscosity of the fluid and $u_{x,y,z}*$ correspond to the friction velocity in the x, y, and z directions obtained closer to the wall, and Δx, Δy, and Δz are the wall distances in the respective directions.

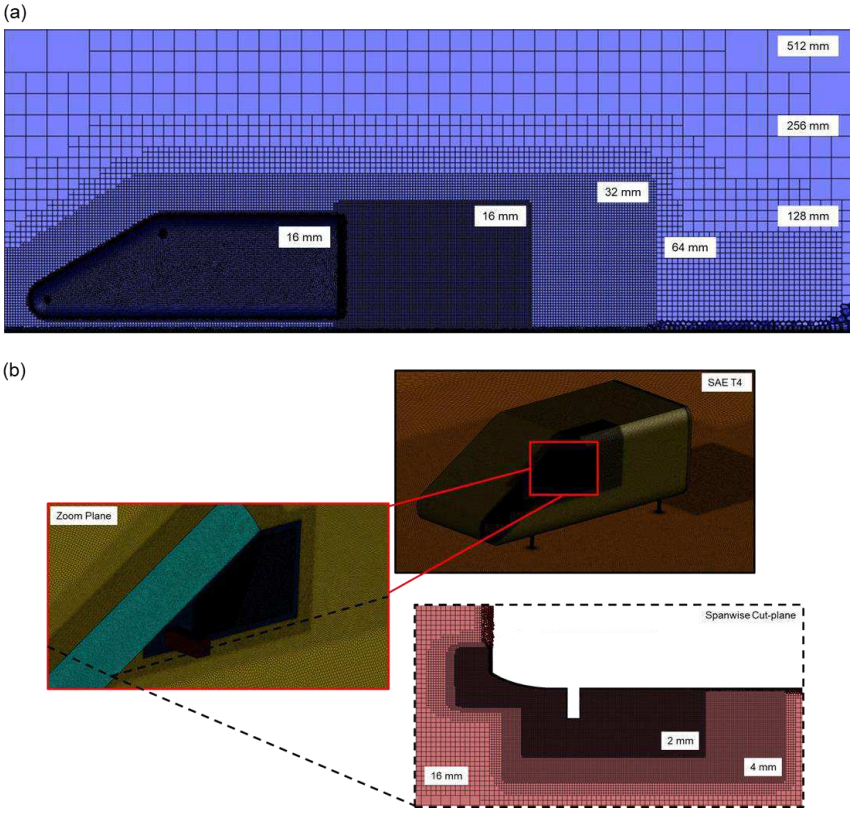

Fig. 3. a) Overview of a medium grid with local refinement zones used for validation study, b) grid generated closer to forebody, side window (zoom plane), and spanwise cut plane.

Table I
Comparison of grid sizes and the aerodynamic force coefficient for SAE T4 with mirror for various grids used in the study

Grid	Wall Normalised Units	Total Cell Count	$Cd_{vehicle}$	$Cl_{vehicle}$
Coarse	$\Delta x^+ =$ 140 – 1200; $\Delta y^+ < 1$; $\Delta z^+ =$ 140 – 1200	4.6×10^6	0.2779	-0.1153
Medium	$\Delta x^+ =$ 70 – 980; $\Delta y^+ < 1$; $\Delta z^+ =$ 70 – 980	24.7×10^6	0.2604	-0.1266
Fine	$\Delta x^+ =$ 70 – 600; $\Delta y^+ < 1$; $\Delta z^+ =$ 70 – 600	63.8×10^6	0.2599	-0.1270

C. Numerical modelling and solution setup

All the cases investigated in the present work were numerically solved using ANSYS Fluent version 2020 R2. An overview of the procedure used to run the numerical simulations is presented in the flowchart in Fig. 4. For all cases, the transient models based on SBES were initialised using a steady-state solution based on the steady-state k–ω SST turbulence model, followed by an unsteady simulation using the SBES-WALE turbulence model for a total runtime of 0.65s. The unsteady simulation was run in three phases: in the first phase, a time step of 1×10^{-4} s was used for the first 0.3s after which the time step was changed to 2.5×10^{-5} s for the next 0.05s to flush out any instability induced by the change in the time step and to ensure that the residual error for the momentum and turbulent equations reached below 1×10^{-6}. The use of two different time steps reduces the computational expense; however, the residual drop is ensured to be less than 1×10^{-6} for all quantities. In the final phase, the time-step was changed to 2.3×10^{-5}s for the next 0.3s to collect time-averaged data. Along with the time-averaged flow data, the pressure fluctuations on the side-view mirror, A-pillar, Frame, and side window were recorded at every time step for the last 0.3s which is later used as an input for the FW-H acoustic analogy. For more details on the SBES and FW-H coupling and solution processes, the readers are directed to the previous publications of Chode *et al.*[2,32]

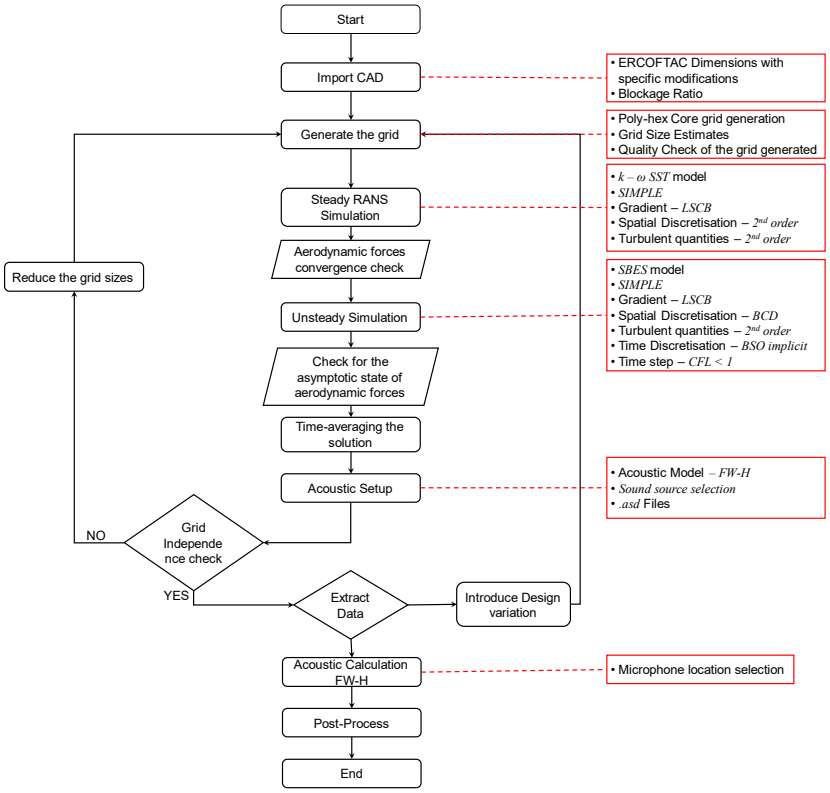

Fig. 4. A flow Chart representing the procedure followed for the simulations performed in this study, along with the numerical methods used.

D. Grid evaluation study

A grid evaluation study is conducted using the SBES turbulence model. To obtain a grid-independent solution, first, the difference in $Cd_{vehicle}$ is obtained from Eq. 2 and the $Cd_{vehicle}$ predicted by the medium and fine grids was <1%, as listed in Table I. The pressure coefficient Cp defined in Eq. 3 was extracted on the cross-section of the side-view mirror at the midplane indicating that both the medium and fine grids predicted Cp had good agreement between them, as shown in Fig. 5. The flow structures obtained on the midplane of the side-view mirror using time-averaged velocity magnitude streamlines for all grids, as shown in Fig. 6, indicate a minimal difference between the predictions made for the medium and fine grids, as shown in Table II.

$$Cd_{vehicle} = \frac{2F_{drag}}{\rho U_\infty^2 F_A}$$
$$Cl_{vehicle} = \frac{2F_{lift}}{\rho U_\infty^2 F_A} \quad (2)$$

Here, $Cd_{vehicle}$, and $Cl_{vehicle}$ represent the coefficient of drag and lift respectively, while F_{drag} and F_{lift} indicate the predicted drag and lift force while F_A, is the frontal area of the vehicle.

$$Cp = \frac{p - p_\infty}{\frac{1}{2}\rho U_\infty} \quad (3)$$

where, p_∞ and p is the static pressure in the freestream and at the point where the pressure coefficient is evaluated respectively and ρ is the density of the fluid in the freestream.

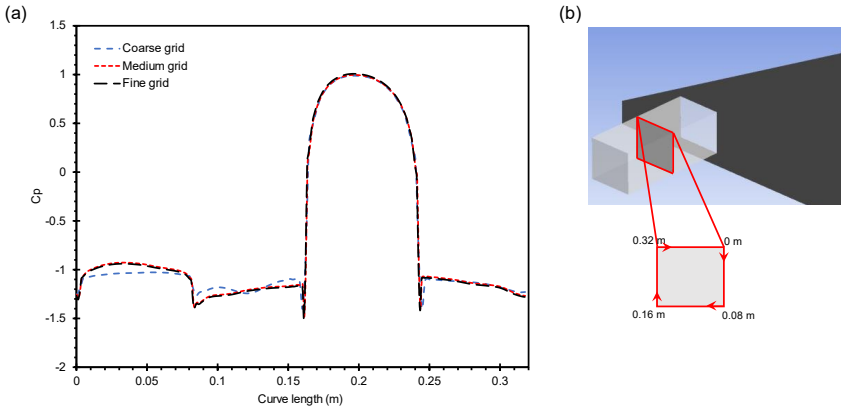

Fig. 5. Comparison of the coefficient of pressure (*Cp*) between the grids used in the study and b) schematic of the location where *Cp* is generated.

Table II
Normalised lengths of the time-averaged flow features compared against the grids used in the study.

Grid	L_{hx}	L_{hz}	L_{ws}	Cd_{svm}
Coarse	1.08 l_c	1.18 l_c	2.92 l_c	0.9312
Medium	1.09 l_c	1.24 l_c	2.98 l_c	0.9753
Fine	1.1 l_c	1.25 l_c	3.01 l_c	0.9702

Additionally, the difference in the mean drag coefficient for the side-view mirror (Cd_{svm}) between the medium and fine grid is <1%. The hydrodynamic pressure fluctuations (HPF) obtained at five different locations on the side window were extracted, as shown in Fig. 7, at the low frequency ranges (f < 100 Hz) the peaks are more pronounced in the predictions

obtained from medium and fine grids with minimal differences in the amplitudes. Similarly, minimal differences are seen in the amplitudes predicted at medium (100 Hz < f < 1000 Hz) and higher frequencies (f > 1000 Hz) for medium and fine grid.

Based on the comparisons, it is evident that a medium grid appears to be more reasonable for this study owing to its prediction capability and lower computational resource requirement; thus, it was used for all cases investigated in this study.

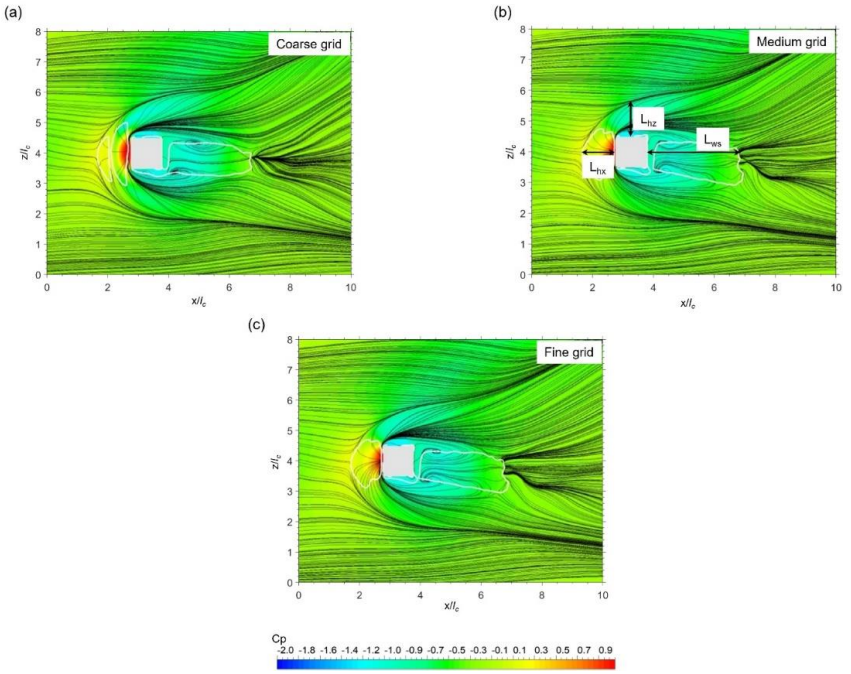

Fig. 6. Comparison of time-averaged velocity magnitude streamlines superimposed on the pressure coefficient generated on a plane at y = 0.01 l_c between a) Coarse grid, b) Medium grid and c) fine grid. L_{hx}, L_{hz}, and L_{ws} represent the normalised length of the horseshoe vortex from the mirror, normalised height of the vortex from the lateral edge of the mirror, and normalised length of the wake structure measured from the rear face of the mirror, respectively.

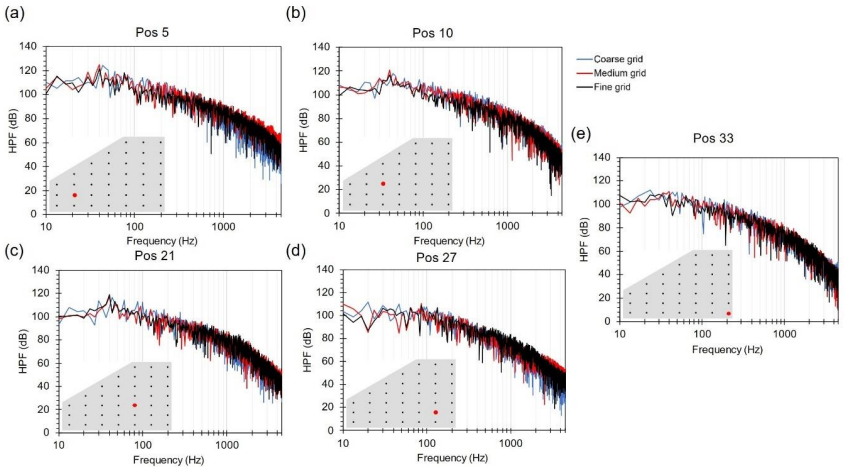

Fig. 7. The hydrodynamic pressure fluctuations (HPF) were extracted from a) Pos5, b) Pos10, c) Pos21, d) Pos27 and e) Pos33 sensors located in the window. The red dot in the schematic represents the location of the probe position where the HPF is plotted (see Fig.1(c) for the number labelling of the sensors on the side window).

RESULTS AND DISCUSSION

A. Comparison of current results against previously published results

The flow visualisation obtained from the SBES prediction is compared with the experimental data presented by Nusser[47] using the wall shear stress distribution on the surface of the SAE T4, as shown in Fig. 8. The SBES predicts the horseshoe vortex formed in front of the side-view mirror and the interaction between the flow past the A-pillar and horseshoe vortex. The location and dimensions of the flow interaction and horseshoe vortex are observed to be in good agreement with the experimental data.

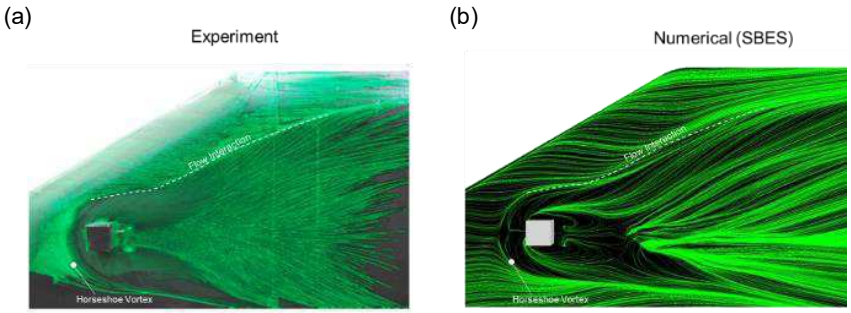

Fig. 8. Comparison of flow patterns on the side of SAET4 a) experimental data[47] and b) numerical prediction obtained from the SBES.

As the flow patterns are in good agreement, a comparison is made between the hydrodynamic pressure fluctuations exerted on the side window using the RMS of the surface pressure fluctuations *p'*. The predicted overall RMS agrees well with the experimental results. At 150 Hz and 500 Hz, the amplitudes of the pressure fluctuations are qualitatively in reasonable agreement with the experiment in reasonable agreement, but the amplitude levels and locations are different in the highlighted regions in Fig. 9(b) and (c). As the frequency increases the pressure fluctuations exerted by the A-pillar flow are dampened (see highlighted region *a* in Fig 9(b) and(c)). Therefore, the influence of A-pillar pressure fluctuations on the side window is limited to low-frequency ranges, and a similar observation is made by Nusser[47] when comparing the numerical results with experiments.

A quantitative comparison is made between the predicted and measured hydrodynamic pressure fluctuations (HPF) as the flow patterns around the side window are in good agreement with the experimental results (See Fig. 10). The HPF was measured at two probe positions where the experiments indicated the presence of aeolian tones at 40 Hz and 80 Hz in Pos1, while in Pos15, the tonal peak was located at 40 Hz and no peak was evident at 80 Hz. The peaks in the experiments correspond to a Strouhal frequency of 40 Hz for the side-view mirror ($St \approx 0.116$), and the Strouhal frequency is obtained from Eq. 4, which corresponds to *St* of a square cylinder. The numerical results also indicated tonal peaks at the same frequency, as shown in Fig. 10. However, the intensity of the HPF predicted for the tonal peaks shows a difference of a maximum of 3-5 dB.

$$St = \frac{f.l_c}{U_\infty} \tag{4}$$

Here, f is defined as the frequency of vortex shedding and l_c is the characteristic length (side of the square) of the square cylinder.

Furthermore, a comparison is drawn to verify the predictions made by SBES with the LES predictions presented by Nusser[47], indicating that the SBES predictions are under-predicted for all sensor locations, as shown in Fig. 11. For sensors located on the side window at Pos1 and Pos2 (See Fig.1 (c) for the number associated with the sensor), which are in the wake of the side-view mirror, there is reasonable agreement between SBES and LES compared to positions Pos20 and 32, as shown in Fig. 11. A difference of ~5-10 dB is seen at low (f < 100 Hz) and medium (100 Hz < f < 1000 Hz) frequencies between the SBES and LES results for all sensor locations. This difference can be attributed to the denser grids used for the side window in LES compared with the grid used for SBES.

Accepted to Phys. Fluids 10.1063/5.0156111

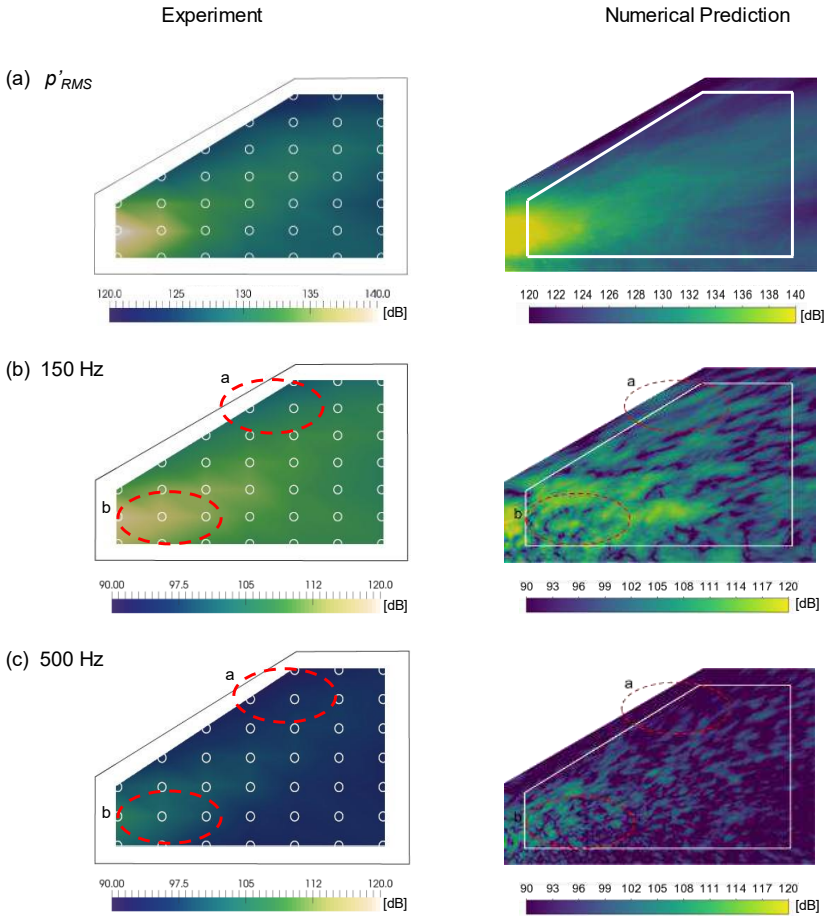

Fig. 9. Comparison of amplitude of pressure fluctuations in dB on the side window between experiment[47] and numerical results for a) p'_{RMS}, b) 150 Hz, and c) 500 Hz. A reference pressure of 2 x10^{-5} pa.

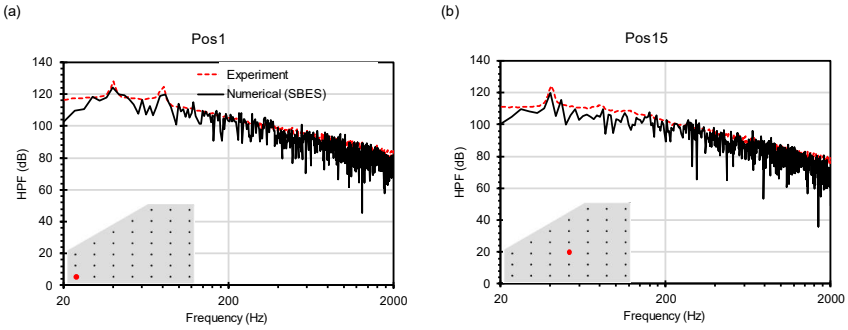

Fig. 10. Comparison of HPF between experiment[47] and numerical (SBES) prediction for sensors a) pos1 and b) pos15. The locations of the sensors are marked with red dots in the schematic of the graph. Refer to Fig. 1(c) shows the number labelling of the sensors on the side window.

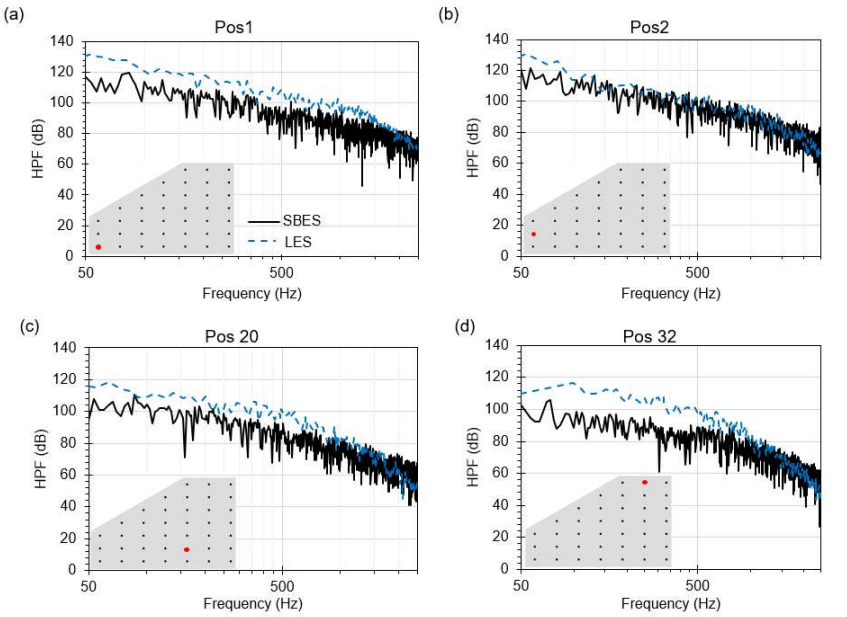

Fig. 11. Comparison between the predictions made by SBES and LES[47] at four different positions in the side view, as illustrated by the red dots in the schematic: a) pos1, b) pos2, c) pos20, and d) pos32. Refer to Fig. 1(c) shows the number labelling of the sensors on the side window.

B. Side-view mirror and its influence on Drag Coefficient and Hydrodynamic pressure fluctuations

The side-view mirror is the major source of noise generation in vehicles; therefore, in this study, simulations were carried out without the mirror (no mirror) to investigate its effects. The drag of the vehicle $Cd_{vehicle}$ is reduced by ~13.13% compared to SAE T4 with a mirror (See Fig. 1(a)), despite the change in the frontal area (F_A) of 0.82% between SAE T4 with and without the mirror (See Table III). From a quantitative comparison of the flow features around SAE T4 with and without a mirror, which is visualised using the instantaneous Q criterion defined in Eq. 5.

$$Q = 0.5 * (\Omega_{ij}\Omega_{ij} - S_{ij}S_{ij}) \quad (5)$$

where Ω_{ij} is the rotation, and S_{ij} is the strain rate.

Based on the observations from Fig.12 (a-b), there is a negligible difference in the length of the vehicle wake predicted in both scenarios. When the side-view mirror is present, the a high concentration of turbulent structures caused by horseshoe vortex in the upstream and the vortex shedding in the wake of the side view mirror are seen closer to the side window and these structures impact the flow originating from the A-pillar. While, in the absence of the side -view mirror, the flow around the A-pillar appears to be smooth without any significant detachment or reattachment, as illustrated in Fig.12 (c-d).

The pressure fluctuations experienced on the side window in the no-mirror case are potentially caused by the highly turbulent flow past the A-pillar, as shown in Fig. 12(d). However, in the mirror case, the pressure fluctuations experienced by the side window is primarily due to vortex shedding in the wake of the mirror, as shown in Fig. 12(c). The normalised pressure fluctuations, Np'_{rms}, shown in Fig. 13, indicate that the side window in the mirror cases experienced pressure fluctuations twice as high as those in the no-mirror case. A similar observation can also be made in the case of the A-pillar, as shown in the highlighted by dotted oval region in Fig. 13.

Table III

Comparison of frontal area (F_A) and drag coefficient ($Cd_{vehicle}$) between SAET4 with and without mirror

Case	Frontal Area (F_A) m^2	% Change in F_A w.r.t mirror case	$Cd_{vehicle}$	% C_{dA} w.r.t mirror case
With Mirror	1.9319	-	0.2604	-
Without Mirror	1.9160	0.82	0.2304	13.13

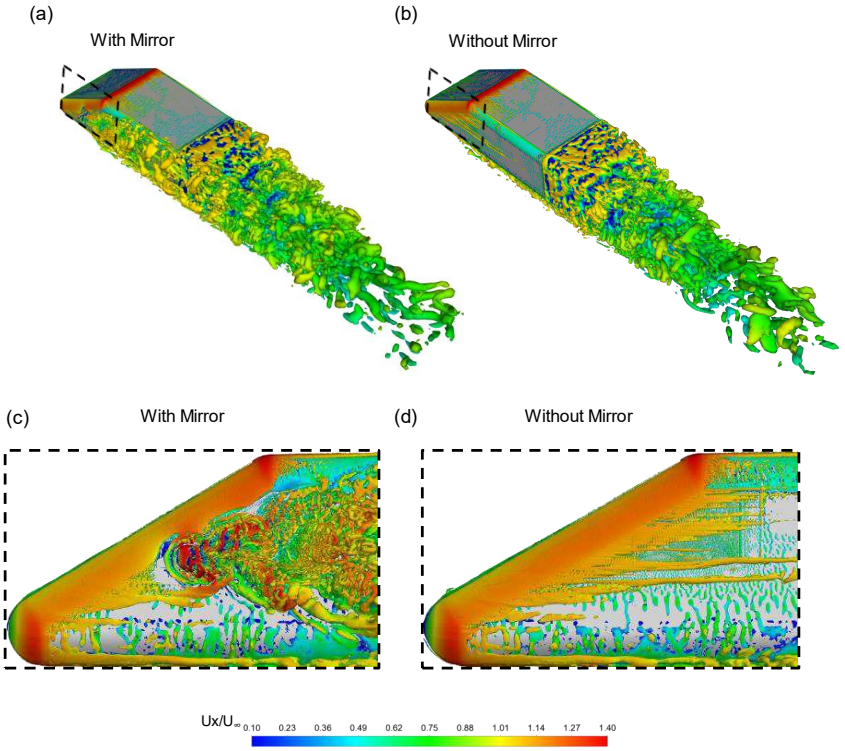

Fig. 12. Comparison of vortical structures of an instantaneous flow field visualised by iso-surfaces of Q = 1100 s^{-2} coloured with instantaneous x-velocity for SAE T4 a) with mirror and b) without mirror, while c) and d) represent the zoomed image of the flow structures around the A-pillar and side window.

Furthermore, the hydrodynamic pressure fluctuations exerted on the side window are reduced by 35 – 65 dB compared to SAE T4 with the mirror case, as illustrated in Fig. 14. The difference predicted in the amplitude at low frequencies is consistent with the results of previous studies.[7,33] The pressure fluctuations exterted on the side window in the no-mirror case are dominant at low frequencies up to 100 Hz, with the peak amplitude predicted at 40 Hz, similar to the mirror case, as shown in Fig. 14.

The Overall Sound Pressure Level (OASPL) is obtained using Eq. 6. The OASPL is measured at two probe positions; probe 1 (1.6m, 0.92m, 1.8m) and probe 2 (2.5m, 0.75m, 4m) from the origin of the vehicle body (See Fig. 1) suggests that the radiated noise decreases from 76.18 dB to 47.95 dB and from 61.63 dB to 31.65 dB, respectively, in the absence of the side-view mirror (See Table IV), and the A-pillar is the highest contributor to the overall noise radiated for both probe positions. Therefore, in the absence of a side-view mirror, the A-pillar is a potential noise source, which is consistent with the findings of Hartmann *et al.*[7], Dawi and Akkermans[34] and Lai *et al.*[49]

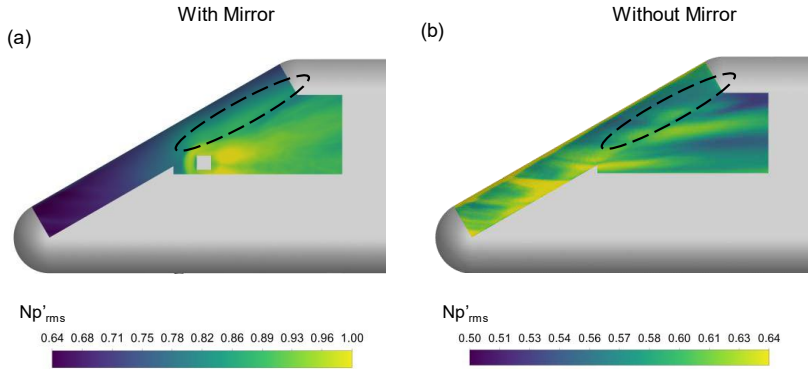

Fig. 13. Comparison of normalised *p'rms* (*Np'rms*) (defined as N*p'rms* = *p'rms/max.p'rms*) where *max.p'rms* = 142.73 dB (predicted from the case with mirror) between a) with mirror and b) without mirror cases. The scales presented are intentionally different due to the level of intensity predicted in both cases. The changes in the pressure fluctuations are highlighted using a dotted oval shape.

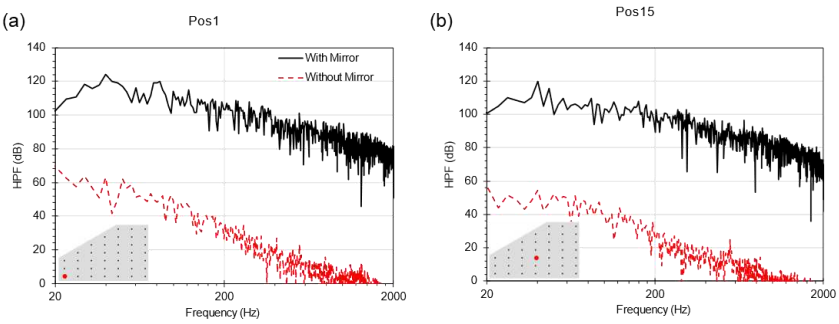

Fig. 14. Comparison of HPF between experiment SAET4 with and without a mirror at sensors a) pos1 and b) pos15. The locations of the sensors are marked with red dots in the schematic of the graph (see Fig.1(c) for the number labelling of the sensors on the side window).

$$p'_{nrms} = \sqrt{\frac{1}{N}\sum_{n=1}^{N}(p'_n)^2}$$
$$OASPL = 10\log_{10}\left(\frac{p'^2_{nrms}}{p^2_{ref}}\right) \quad (6)$$

Where, p'_n is the sound pressure obtained at the probe position and N is the number of samples.

Table IV
Comparison of noise radiated from SAE T4 with mirror and without mirror. The units for the values presented are in dB

	A-Pillar		Side window		Frame		OASPL	
	Probe 1	Probe 2	Probe 1	Probe 2	Probe 1	Probe 2	Probe 1	Probe 2
No Mirror	41.65	25.52	39.60	23.41	33.34	17.55	47.95	31.65
With Mirror	68.35	54.32	74.33	61.23	73.61	61.03	76.18	61.63

C. Effects of inclining the mirror on the aerodynamic characteristics of SAE T4

In this study, the inclination of the mirror (θ) is defined as shown in Fig. 15. Hereafter, the mirror side is represented as w_m, whereas the side without a mirror is referred to as w'_m, as shown in Fig. 15. The $Cd_{vehicle}$ for various angles shows a constant decrease in the overall drag of SAE T4, except at 24°, where $Cd_{vehicle}$ increased by ~ 2.8% compared to 16°. Also, SAE T4 with mirror mounted at 16° reports the lowest drag configuration as shown in Table V. A similar trend is observed in Cd_A evaluated at the base of the vehicle. Cd_A was evaluated as shown in Eq. 7, which is also referred to as '*micro drag*' by Cho *et al.*[45] and Hucho[46]. In Eq. 7 first term correspond to the total pressure loss, the second term corresponds to the momentum deficit, and the last term represents the swirl drag, respectively. The overall lift coefficient tends to decrease up to 16°, after which SAE T4 experiences less downforce, with $Cl_{vehicle}$ being the lowest at 32°.

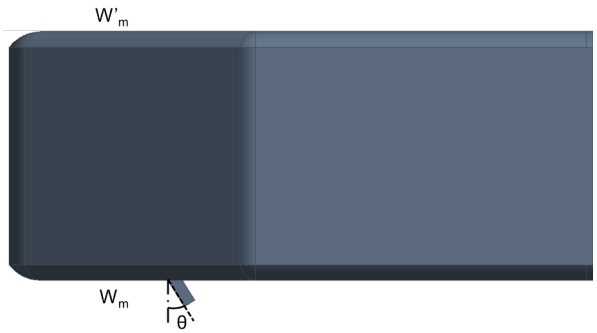

Fig. 15. Schematic of inclination of the mirror. Here, θ was varied from 0° to 32° in intervals of 8°. w_m and w'_m represent the sides with and without a mirror, respectively.

$$Cd_A = \int_s (1 - C_{p,tot})dS - \int_s \left(1 - \frac{u}{U}\right)^2 dS + \int_s \left[\left(\frac{v}{U}\right)^2 + \left(\frac{w}{U}\right)^2\right] dS \tag{7}$$

Table V
Comparison of force coefficients and pressure coefficients on the base between all the inclination angles (θ) investigated in this study.

Inclination Angle (θ)	$Cd_{vehicle}$	$Cl_{vehicle}$	$Cd_{A\ @base}$
0°	0.2604	-0.1187	0.2041
8°	0.2554	-0.1191	0.2037
16°	0.2489	-0.1197	0.2001
24°	0.2562	-0.1180	0.2082
32°	0.2493	-0.1074	0.2026

To further investigate the behaviour of drag, Cp on the base of SAE T4 for all θ is analysed along with the structure of the wake obtained using the iso-surface of the time-averaged mean total pressure, $Cp_{,tot}$ = -0.2, as shown in Fig. 16. $Cp_{,tot}$ is obtained using Eq. 8.

$$Cp_{,tot} = \frac{p_{tot} - p_{ref}}{\frac{1}{2}\rho U_\infty^2} \tag{8}$$

where p_{tot} is the total pressure, and p_{ref} is the reference pressure considered as 1atm.

$$Fs = \oint p\, dA$$
$$C_s A = \frac{2 * Fs}{\rho * U_\infty^2} \tag{9}$$

Generic flow structures behind the squareback form a circular vortex ring as evidenced by Rouméas *et al.*[52], Pavia[53], and Bonnavion *et al.*[54], a similar structure is predicted for all inclination angles. The vortex ring is a combination of the flow emanating from the roof, underbody, and sidewalls of the body which separate from the rear edges of the base of the square and together form a circular vortex ring. However, the circular vortex ring shape is affected when θ varies. For $\theta = 0°$ to 16°, the flow emanating from the w_m side is dominant, as indicated in Fig.16 (a) – (c), whereas the flow from the w'_m side tends to be less separated at the left edge of the base of the vehicle, which increases with an increase in θ from 0° to 16°. From the iso surface plots of the mean $Cp_{,\,tot}$, it is evident that the flow from w_m deflects the wake towards the w'_m side. With an increase in θ, the movement of the wake towards the w'_m side decreased until $\theta = 16°$. In addition, the low-pressure footprint seen on the base is dominant on the w_m side and roof of SAE T4. With an increase in the inclination angle from 0° to 16°, the low-pressure footprint tends to become smaller and concentrated closer to the w_m side of the body.

At 24°, the circular vortex ring formed indicates more flow emanating from the roof compared to θ = 0°–16° which is also indicated by the low-pressure footprint tending to decrease in magnitude and size compared with other angles from 0° to 16°, as shown in Fig. 16 (d). The negative pressure region from closer to the roof of SAE T4, while the low-pressure footprint on the w_m side decreased in both size and magnitude. A similar observation can be made for the 32° case (see Fig. 16 (e)), where a low-pressure footprint is formed closer to the roof but spreads between the lateral edges of SAE T4. This can be attributed to the decrease in the effect of mirror-induced vortices on the wake of the vehicle.

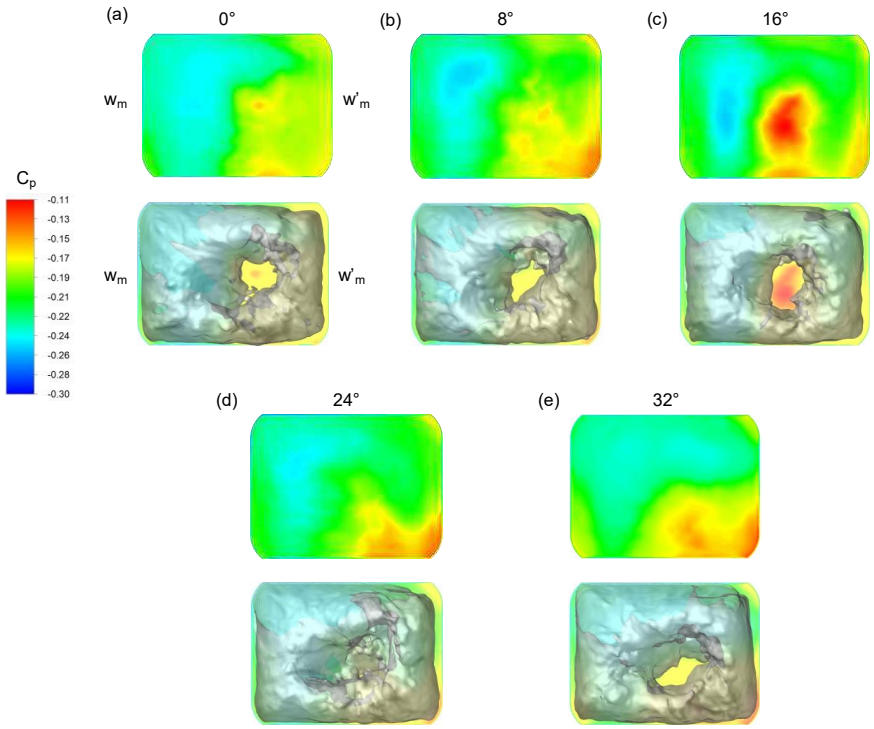

Fig. 16. Comparison of the coefficient of pressure at the base of SAE T4 (top) and the wake structure near the base visualised by the generated iso-surface of the mean total pressure $Cp_{,tot}$ = -0.2 (bottom) between a) 0°, b) 8°, c) 16°, d) 24° and e) 32°.

From Fig. 16, it can be observed that the flow behaviour on the side governs the behaviour of the low-pressure region on the base. The forces exerted on the sides of SAE T4 were calculated using Eq. 9, adjusting for direction, and are summarised in Table VI to identify the consequence of inclining the mirror on the force coefficients of SAE T4. The w_m side experiences a higher side force than the w'_m side for all the cases investigated in this study. The increase on the w_m side is attributed to the reattachment of the flow separated from the mirror on the w_m side of SAE T4. In addition, a constant decrease in the side force of the w_m side implies that with a change in θ, the reattachment of the flow on the side of SAE T4 is reduced which is visualised using the direction of the shear layer using streamlines and vorticity plots. Fig. 18 indicates that after $\theta = 16°$, the shear layer from the lateral edge of the mirror becomes parallel to the side of SAE T4, resulting in less side force on the w_m side (See Table VI).

Table VI
Comparison of difference obtained for the *CsA* evaluated at the mirror side (w_m) and no mirror side (w'_m) between all the angles investigated.

Inclination Angle (θ)	w_m	w'_m	Difference in %
0°	0.1883	0.1711	9.58
8°	0.1875	0.1715	8.86
16°	0.1858	0.1729	7.19
24°	0.1854	0.1723	7.31
32°	0.1818	0.1716	5.40

The difference in side force causes an imbalance which results in the formation wake which is dominant towards the left side of the vehicle, as indicated by the circular vortex ring in Fig. 16. The imbalance in the force reduces the overall drag experienced by the vehicle, as shown in Tables V and VI for θ = 0° to 16°. When the imbalance increases, the overall drag also increases, as observed in the predicted $Cd_{vehicle}$ for θ = 24°. For 32°, the imbalance again decreases and is also the lowest among all cases. Therefore, it appears that the imbalance in the side force is proportional to the overall drag of the vehicle, and the relationship tends to be linear, as shown in Fig. 17.

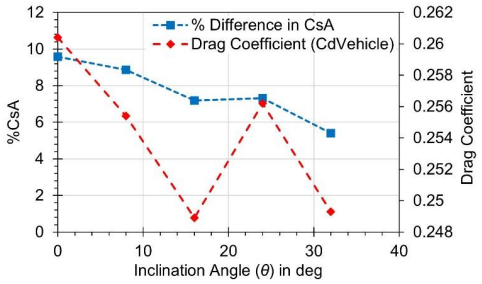

Fig. 17. Relationship between % difference in side forces and drag coefficient of vehicle ($Cd_{vehicle}$) with respect to inclination angle (θ).

Accepted to Phys. Fluids 10.1063/5.0156111

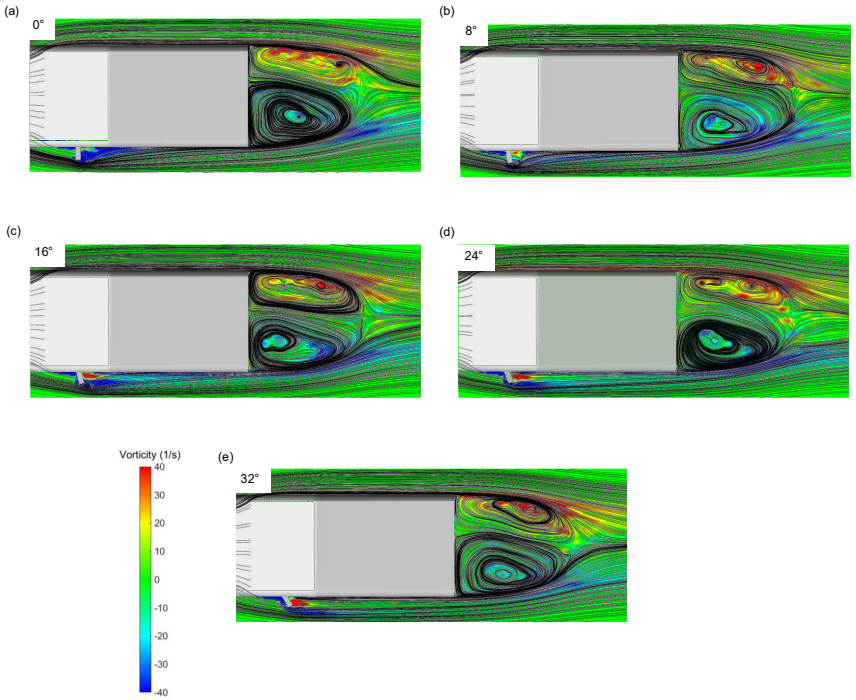

Fig. 18. Comparison of time-averaged vorticity contours superimposed with velocity streamlines on the midplane of the side-view mirror at $y/H = 0.68$ between a) 0°, b) 8°, c) 16°, d) 24°, and e) 32°.

For SAE T4 with a mirror mounted at $\theta = 0°$, there are two vortices (V_1 and V_2), as shown in Fig. 19, which are formed because of flow separation from the top and bottom trailing edges of the side view mirror, which tend to diverge from each other as they traverse towards the base of the body. Vortex V_1 tends to affect the flow not only from the side but also from the roof, as shown in Fig. 19 (a), whereas V_2 tends to affect the underbody flow. This divergence of the vortex decreases with an increase in θ of the mirror up to 16°. A further increase in $\theta = 24°$ results in the formation of a single vortex V_1 which is weaker than the other V_1 vortices, as shown in Table VII. However, for $\theta = 32°$ even though a single vortex is formed the strength of the vortex is higher than that at 24°. This difference can be attributed to flow separation at the mirror. For $\theta = 0°$- 16°, the flow separated from the top and bottom faces of the mirror, while for the 24° and 32°, the flow separation is more pronounced from the lateral face of the mirror which is evident in the mean averaged vorticity plot presented in Fig. 18.

Accepted to Phys. Fluids 10.1063/5.0156111

Table VII
Comparison of the vortex strength evaluated at streamwise planes between all the sweep angles investigated. All the values presented for vortex strength have units of '1/s'

θ	$x/L = 0.48$	Vortex definition	$x/L = 0.97$	$x/L = 1.05$	$x/L = 1.13$	$x/L = 1.21$
0°	3.1665	V_1	9.7561	28.9742	30.8604	23.8382
		V_2	-6.4112	-6.2319	-6.40352	-5.2130
8°	3.1172	V_1	9.7499	26.7323	28.7230	23.6986
		V_2	-6.5876	-5.1707	3.9549	3.499
16°	3.0781	V_1	8.0646	24.8017	23.8061	23.6664
		V_2	-0.1146	11.2560	17.6937	0.5103
24°	6.0164	V_1	2.1608	15.5168	16.7498	11.3650
		V_2	-	-	-	-
32°	5.4167	V_1	3.9709	16.7444	19.9076	9.2496
		V_2	-	-	-	-

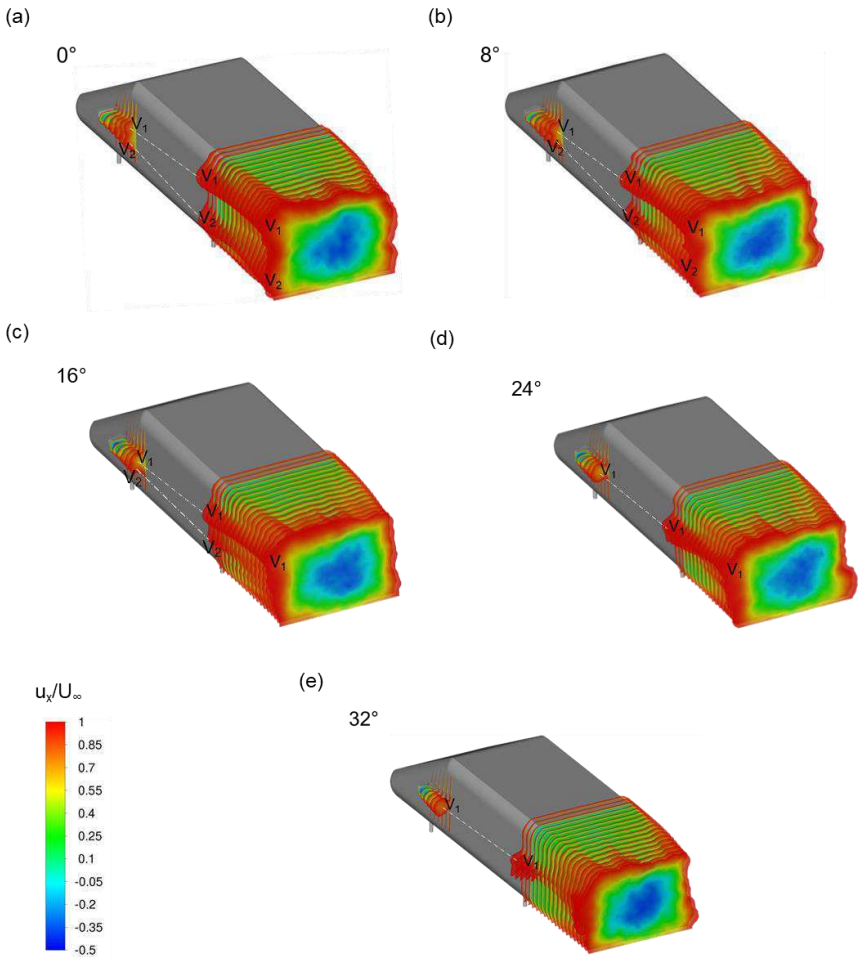

Fig. 19. time-averaged velocity magnitude plotted in the wake of the mirror and SAE T4 for θ = a) 0°, b) 8°, c) 16°, d) 24°, and e) 32°. V_1 and V_2 represent mirror-induced vortices emerging from the top and bottom faces of the mirror, respectively.

D. Effects of inclining the mirror on the acoustic characteristics of SAE T4

The effect of inclining the mirror on the flow structures around the forebody is shown using the time-averaged wall shear stresses in Fig. 20. A horseshoe vortex is formed where the mirror is mounted on the side of SAE T4, similar to the half-round mirror mounted on a flat plate. [1,2,24,29,55] However, the horseshoe vortex predicted for all inclination angles (θ) is asymmetric in the normal direction, in contrast to observations made in flat-plate cases[2]. The horseshoe vortex dimensions tend to decrease with an increase in θ which is in line with the predictions

made for isolated inclined mirror cases studied by Chode *et al.*[2], Ask and Davidson[24] and Yao *et al.*[1], as summarised in Table VIII. L_{hx}, L_{hy+}, L_{hy-}, and L_{ws} represent the normalised length of the horseshoe vortex from the mirror, the normalised height from the lateral edge of the mirror, the normalised height of the horseshoe vortex in the positive y-direction, the normalised height of the vortex in the negative y-direction, and length of the wake structure measured from the rear of the mirror, respectively. In addition, α represents the angle between the flow interaction line and A-pillar. A flow interaction line is defined where the flow from the A-pillar interacts with the side-view mirror horseshoe vortex (Fig. 8(b)).

Table VIII
Comparison of the change in the angle made between A-pillar and streamline (α) and the normalised lengths of time-averaged flow feature with the change in θ

Sweep angle (θ)	L_{hx}	L_{hy+}	L_{hy-}	L_{ws}	Change in α w.r.t to 0°
0°	1.348D	1.117D	1.7175D	3.169D	-
8°	1.276D	1.221D	1.575D	3.185D	14.27%
16°	1.212D	1.237D	1.531D	3.067D	23.22%
24°	1.165D	1.088D	1.282D	3.023D	30.09%
32°	0.975D	0.924D	1.087D	2.315D	44.75%

Accepted to Phys. Fluids 10.1063/5.0156111

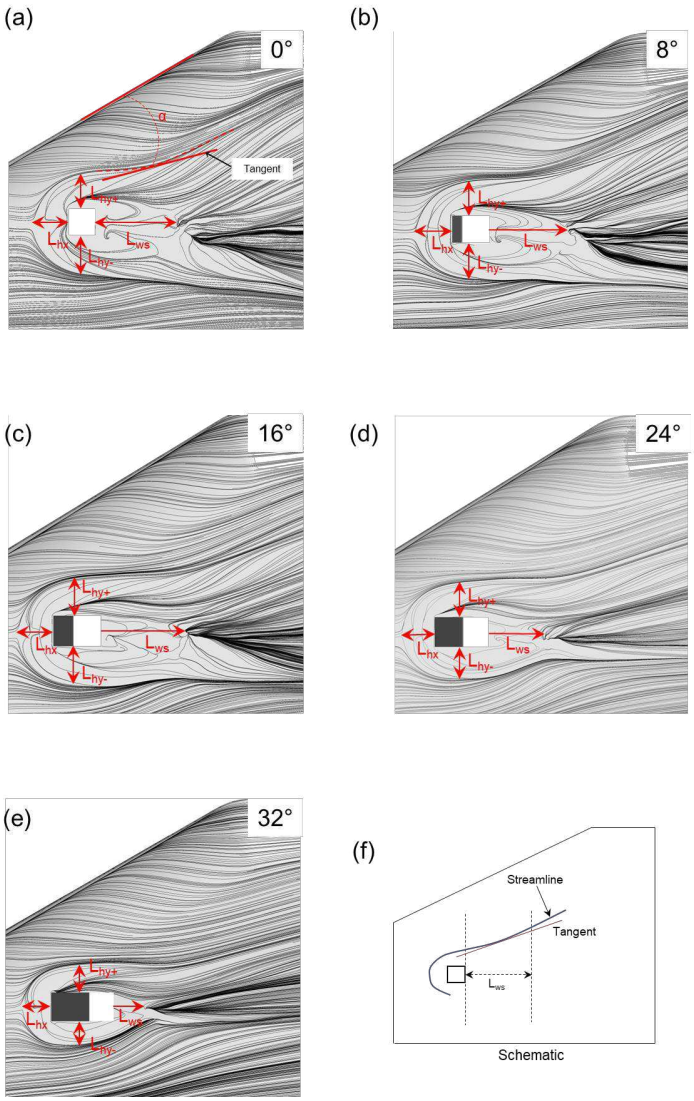

Fig. 20. Comparison of time-averaged wall shear stresses on the forebody of SAE T4 with varying sweep angles: a) 0°, b) 8°, c) 16°, d) 24°, and e) 32°. f) shows the method used to obtain a tangent to the streamline.

In addition, the wake formed behind the mirror decreased with an increase in θ, as indicated by L_{ws} in Table VIII. The angle α between the flow interaction line (as defined in Fig. 8 (b)) and the A-pillar increases with an increase in θ, indicating a decrease in the width of the horseshoe

vortex. Consequently, the pressure fluctuations exerted on the side window are concentrated closer to the mirror wake, as shown in Fig. 21.

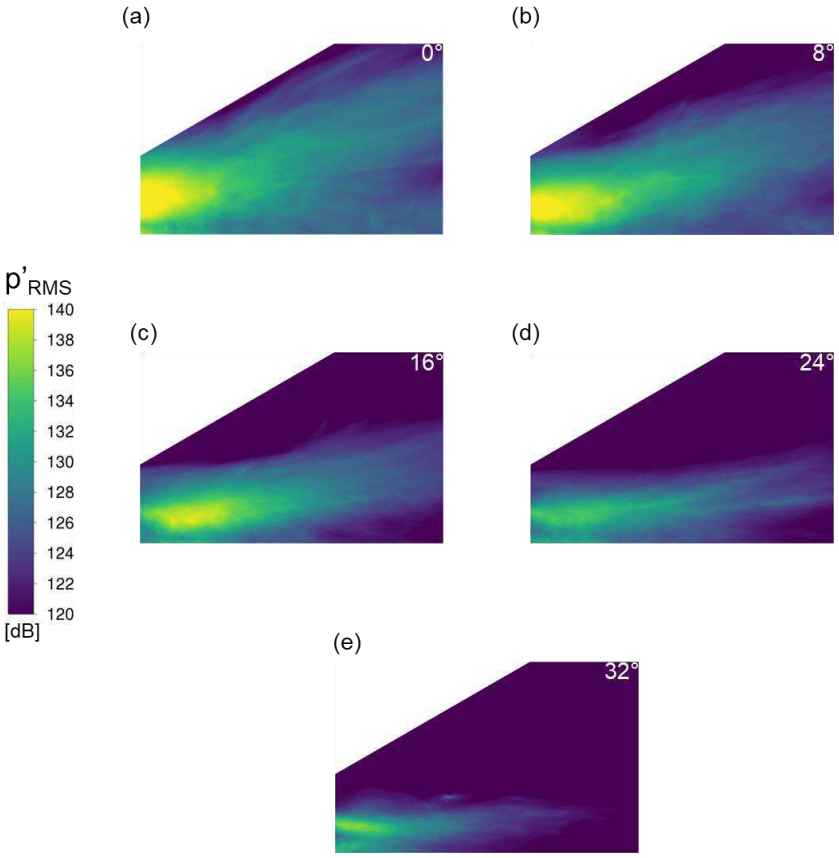

Fig. 21. Comparison of RMS of pressure fluctuations in dB on the side window for a) 0°, b) 8°, c) 16°, d) 24°, and e) 32°.

The pressure fluctuations on the side window are presented using the RMS of the pressure in Fig. 21, where the pressure fluctuations exerted on the side window are reduced when θ is increased which is in accordance with the observations made by Chode *et al.*[2] for isolated inclined mirrors. To quantify this decrease, the HPF is obtained using two surface probes located on the side window (see Fig. 22), where aeolian tones were observed (ref: Fig. 10). The amplitudes of the aeolian tones at 40 Hz and 80 Hz decreased as the mirror inclination angle increased, which can be attributed to the amount of flow interacting with the surface of the side window. As θ increased, the flow tends to separate more from the outboard faces of the mirror,

which, if not reattached to the surface of the side window, leads to a decrease in the overall HPF, as evidenced by the decrease in the magnitude of the RMS of the pressure fluctuations presented in Fig. 22.

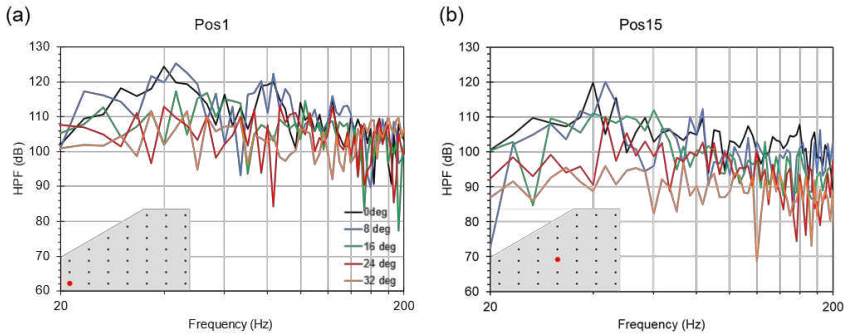

Fig. 22. Comparison of the HPF between all sweep angles investigated at specific sensor locations is illustrated by the red dot in the schematic for a) pos1 and b) pos15. Refer to Fig.1(c) shows the number labelling of the sensors on the side window.

As a result, the noise propagated from the vehicle when evaluated using FW-H at 1.8m and 4 m away from the vehicle, shows a consistent decrease in the Overall Sound Pressure Level (OASPL) when the inclination angle of the mirror is increased, as shown in Table IX. The contribution from each source, such as the side window, side-view mirror, A-pillar, and frame of SAE T4, is shown in Fig. 23. As shown in Fig. 23, the contribution from the surface pressure fluctuation exerted on the side window is the major contributor to the overall noise, whereas the side-view mirror contributes the least when measured at Probes 1 and 2. The contribution of the side-view mirror to the overall noise is reduced with an increase in the θ, and the lowest dB is reported for θ = 16°. In addition, directivity plots were plotted in the vicinity of the side-view mirror and away from the geometrical influence of the sources to evaluate the effect of θ on the structure of the radiated noise.

Table IX
Comparison of noise radiated OASPL (dB) in the vicinity of SAE T4 for all the sweep angles investigated.

Probe location	0°	8°	16°	24°	32°
Probe 1	76.18 dB	73.48 dB	70.73 dB	69.20 dB	67.11 dB
Probe 2	61.63 dB	59.80 dB	57.44 dB	55.83 dB	54.06 dB

Accepted to Phys. Fluids 10.1063/5.0156111

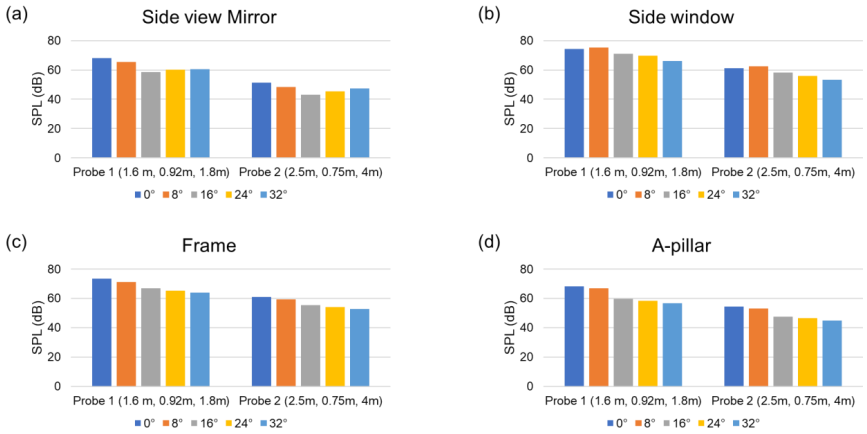

Fig. 23. Component-wise comparison of SPL evaluation at two probes positioned away from SAE T4. a) Side-view mirror, b) side window, c) frame and d) A-pillar.

Fig. 24 and 25 show the directivities of the noise radiating from the sources for the SAE T4 body with inclined mirrors. The OASPL was evaluated at four different planes located at z = 0.56W, 0.62W, 1.13W and 2.5W, and 36 probes were arranged to form a circle with the axis centre of the mirror as the centre of the circle. At each plane, the directivity is obtained using FW-H with a single source (side-view mirror) and all sources (side-view mirror, side window, frame, and A-pillar). At z = 2.5W, located away from the vehicle in the free stream region, the noise radiated patterns resemble a monopole for all the angles investigated for all the sources with 32° predicting the lowest noise levels. For a single source, the radiated pattern is a monopole, but the intensity levels are lower than the dB levels predicted for all sources. The lowest noise radiated for a single source is 16° which agrees with the observations made in Fig. 23. As the measuring plane moves closer to the vehicle, at z = 1.13W, for a single source, 0° and 8° indicate a monopole-like pattern, whereas other angles preserve the monopole pattern which is in contrast to the observations made for all sources in the same plane, where the radiated pattern is monopole.

Probing closer to the vehicle, the radiated pattern changes from a monopole shape, typical of a single noise source, to a cardioid-like shape, indicative of multiple high-intensity noise sources, including the side window (as shown in Fig. 23(b)). The formation of a cardioid-like shape can be attributed to the combination of noise sources. Although the radiated pattern may resemble a dumbbell shape, which is commonly classified as a dipole, the shape predicted for 0° and 8° with a single source does not exhibit a strong representation of a dumbbell-like

shape. Previous studies conducted by Ask and Davidson[56], Becker *et al.*[14], Nusser *et al.*[57], and Chode *et al.*[2] classify the noise source closer to the side window as a dipole, and therefore, the pattern predicted for 0° and 8° can be assumed to have a dipole-like structure. From Fig. 24 and 25, the lowest radiated noise is recorded at 32° for all angles obtained using a single source and all sources, but the maximum reduction is observed for θ = 16°, which agrees with the observations made for OASPL in Table IX. Additionally, the directivity patterns suggest that the noise measured away from the vehicle sources can be considered monopole, which is useful for tests such as pass-by-noise-like scenarios, evaluating the risk for pedestrians from electric vehicles, and optimizing the placement of noise barriers for roads.

In summary, SAE T4 with 16° seems to have low drag and low noise configurations, as the reported drag for 16° is the lowest and the noise radiated is decreased by approximately 10 dB. This study also showed that there is no linear relationship between radiated noise and aerodynamic drag. This study found that the noise emitted is dependent on how the flow behaves closer to the mirror, whereas the consequence of the flow behaviour around the mirror and its interaction with the wake of the vehicle defines the drag. The observations from this study can potentially be extended by replacing the bluff with a mirror with more realistic mirror shapes and the A-pillar is modified to include a rain gutter (a real representation). In addition, the mirror is mounted on only one side of the body in this study due to the availability of experimental data, a fully symmetrical case with similar modifications can add more knowledge to the existing literature.

Accepted to Phys. Fluids 10.1063/5.0156111

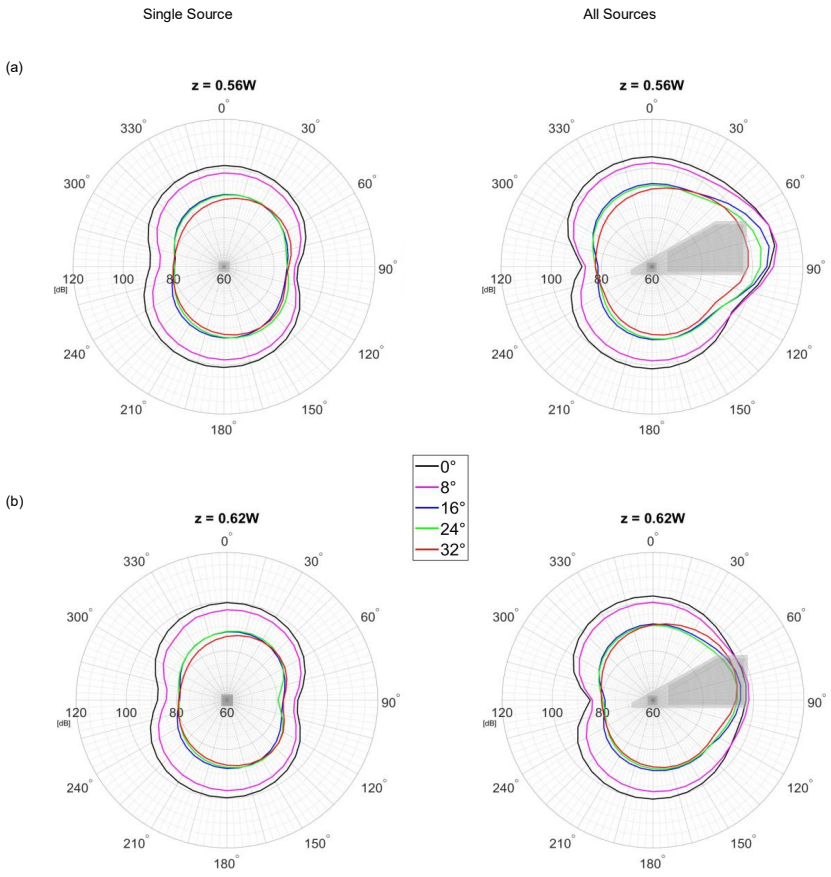

Fig. 24. Directivity plot comparison among all sweep angles investigated at a) z = 0.56 *W* and b) 0.62 *W*. On the left, a single source is used to evaluate directivity, while on the right, all the sources are selected.

Accepted to Phys. Fluids 10.1063/5.0156111

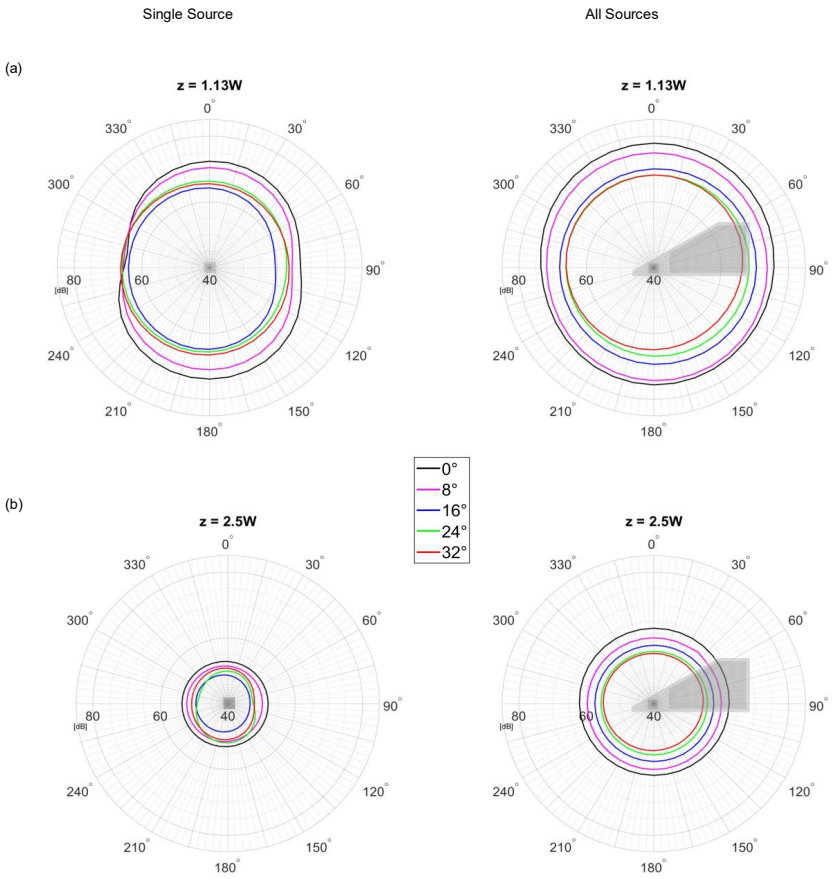

Fig. 25. Directivity plot comparison amongst all the sweep angles investigated at a) z = 1.13 *W* and b) 2.5 *W*. On the left, a single source is used to evaluate directivity, while on the right, all the sources are selected.

Accepted to Phys. Fluids 10.1063/5.0156111

CONCLUSION

A numerical investigation was conducted to predict the noise generated and propagated from a standard squareback body with a bluff mirror mounted on one side of the body. A detailed study of the aerodynamic and acoustic characteristics of the SAE T4 body was conducted using a stress-blended eddy simulation (SBES) coupled with the Ffowcs-Williams and Hawkings (FW-H) analogy. The major conclusions are as follows:

i) An assessment of the SBES coupled with FW-H was presented by validating and verifying the results predicted against the experimental results. The obtained predictions are in good agreement with the experimental results; specifically, the aeolian tones present in the hydrodynamic pressure fluctuation data are captured with a difference of ~ 3-5 dB when compared to the experimental data presented by Nusser[47]. Furthermore, the predicted results are compared against the LES data presented by Nusser[47], where a difference of ~ 5-10 dB is observed in the low- and mid-frequencies.

ii) The influence of the mirror on the aerodynamic and acoustic characteristics of the vehicle is investigated. The numerical predictions suggest that removing the mirror significantly decreases the overall drag, despite the difference in the projected frontal area being minimal, which is expected. However, there is a significant difference in the acoustic characteristics, as the flow past the A-pillar induces pressure fluctuations on the side window which are pronounced at low frequencies (< 100 Hz) with distinct peak amplitudes at a frequency of 40 Hz, corresponding to the vortex shedding frequency of the mirror.

iii) When the mirror inclinations (θ) are varied, the aerodynamic force coefficients show that minimal drag is experienced by SAE T4 at 16°, while at 24°, the drag coefficient increases. A further increase in θ to 32° resulted in a reduction of drag. This study observed a linear relationship between the imbalance in side force coefficient and the drag coefficient of the vehicle. This imbalance arises from the separated flow from the mirror reattaching to the side surface of the vehicle body and the vortices induced by the mirrors. Additionally, the mirror-induced vortices propagate towards the rear end of the vehicle, impacting its wake. The probable explanation for the 16° reporting the lowest drag is attributed to a more balanced flow emanating from the base, leading to a pronounced high-pressure footprint observed on the base.

iv) Although the observed trend in the drag coefficient is not linear with increase in the inclination angle, the radiated noise from SAE T4 decreases as the mirror's inclination angle increases. As θ increases, the pressure fluctuations experienced by the side window tend to

decrease. With the presence of a mirror, the side window emits a greater amount of overall noise compared to a configuration without a mirror. This is because the side window experiences more pressure fluctuations due to the vortex shedding from the side-view mirror and the interplay between the A-pillar and the side-view mirror, making it a significant contributor to the external noise.

v) In this study, when the single source is considered for 0° and 8°, the structure of the radiated noise near the vehicle is dipole-like, which eventually transforms into a monopole when probed further away from the vehicle. For higher inclination angles, the radiated noise maintains a consistent monopole structure, unaffected by the distance to the receiver. However, when multiple sources are taken into consideration, the structure of the radiated noise near the vehicle appears to be less distinctly identifiable as a dipole-like pattern for all cases examined. Nevertheless, when measured away from the body, the radiated noise exhibits a clear monopole structure.

The observations resulting from the study reveal a linear relationship between θ and both L_{ws} and α, a correlation between mirror-induced vortices and overall drag, and a non-linear behaviour relating drag and radiated noise. These findings offer crucial insights for optimisation studies, emphasising the intricate flow interactions associated with mirror inclinations.

ACKNOWLEDGEMENTS

The authors would like to thank Mr. Tushar Jadhav from ANSYS for providing his insights and feedback in the preliminary stages of this work and are very grateful to ANSYS for the Academic Research Partnership Grant. This work was supported by a Vice-Chancellor's PhD scholarship from Sheffield Hallam University and HORIBA MIRA Ltd.

DATA AVAILABILITY

The data that support the findings of this study are available from the corresponding author upon reasonable request.

REFERENCES

[1] H.D. Yao, and L. Davidson, "Generation of interior cavity noise due to window vibration excited by turbulent flows past a generic side-view mirror," Phys. Fluids **30**(3), **036104** (2018). https://doi.org/10.1063/1.5008611

[2] K.K. Chode, H. Viswanathan, and K. Chow, "Noise emitted from a generic side-view mirror with different aspect ratios and inclinations," Phys. Fluids **33**(8), **084105** (2021). https://doi.org/10.1063/5.0057166

[3] R. Camussi, and G.J. Bennett, "Aeroacoustics research in Europe: The CEAS-ASC report on 2019 highlights," J. Sound Vib. **484**, **115540** (2020). https://doi.org/10.1016/j.jsv.2020.115540

[4] Y. He, R. Wan, Y. Liu, S. Wen, and Z. Yang, "Transmission characteristics and mechanism study of hydrodynamic and acoustic pressure through a side window of DrivAer model based on modal analytical approach," J. Sound Vib. **501**, **116058** (2021). https://doi.org/10.1016/j.jsv.2021.116058

[5] T. Li, "Literature review of tire-pavement interaction noise and reduction approaches," J. Vibroengineering **20**(6), **19935** (2018). https://doi.org/10.21595/jve.2018.19935

[6] M.S. Qatu, "Recent research on vehicle noise and vibration," Int. J. Veh. Noise Vib. **8**(4), **051536** (2012). https://doi.org/10.1504/IJVNV.2012.051536

[7] M. Hartmann, J. Ocker, T. Lemke, A. Mutzke, V. Schwarz, H. Tokuno, R. Toppinga, P. Unterlechner, and G. Wickern, " Wind noise caused by the side-mirror and a-pillar of a generic vehicle model, " AIAA Paper No. **2012-2205**, 2012. https://doi.org/10.2514/6.2012-2205.

[8] R.S. Ganuga, H. Viswanathan, S. Sonar, and A. Awasthi, "Fluid-structure interaction modelling of internal structures in a sloshing tank subjected to resonance," Int. J. Fluid Mech. Res. **41**(2), 145–168 (2014). https://doi.org/ 10.1615/InterJFluidMechRes.v41.i2.40

[9] V. Jadon, G. Agawane, A. Baghel, V. Balide, R. Banerjee, A. Getta, H. Viswanathan, and A. Awasthi, "An experimental and multiphysics based numerical study to predict automotive fuel tank sloshing noise," SAE Tech. Pap. **1**, **2014-01-0888** (2014). https://doi.org/10.4271/2014-01-0888

[10] S.J. Elliott, "Active control of structure-borne noise," J. Sound Vib. **177**(5), **1459** (1994). https://doi.org/10.1006/jsvi.1994.1459

[11] M. Helfer, "General aspects of vehicle aeroacoustics," in Proceedings of the Lecture Series

on Road Vehicle Aerodynamics (Von Karman Institute, Rhode-Genèse, Belgium, 2005) (2005).

[12] H. Yuan, Z. Yang, Y. Wang, Y. Fan, and Y. Fang, "Experimental analysis of hydrodynamic and acoustic pressure on automotive front side window," J. Sound Vib. 476, **115296** (2020).https://doi.org/10.1016/j.jsv.2020.115296.

[13] K. Nusser, and S. Becker, "Numerical investigation of the fluid structure acoustics interaction on a simplified car model," Acta Acust. **5**(4), **22** (2021). https://doi.org/10.1051/aacus/2021014

[14] S. Becker, K. Nusser, and M. Oswald, "Aero-Vibro-Acoustic Wind Noise-Simulation Based on the Flow around a Car," SAE Tech. Pap. **1**, **2016-01-1804** (2016). https://doi.org/10.4271/2016-01-1804

[15] B. Levy, and P. Brancher, "Topology and dynamics of the A-pillar vortex," Phys. Fluids **25**(3), **125103** (2013). https://doi.org/10.1063/5.0070092

[16] N. Ashton, A. West, S. Lardeau, and A. Revell, "Assessment of RANS and DES methods for realistic automotive models," Comput. Fluids **128**, **1-15** (2016). https://doi.org/10.1016/j.compfluid.2016.01.008

[17] E. Guilmineau, G.B. Deng, A. Leroyer, P. Queutey, M. Visonneau, and J. Wackers, "Assessment of hybrid RANS-LES formulations for flow simulation around the Ahmed body," Comput. Fluids **176**, **302-319** (2018). https://doi.org/10.1016/j.compfluid.2017.01.005

[18] C. Li, S. Tang, Y. Li, and Z. Geng, "A Modified RANS Model for Drag Prediction of Practical Configuration with Riblets and Experimental Validation," Aerospace **9**(3), **1-25** (2022). https://doi.org/10.3390/aerospace9030125

[19] C. Read, and H. Viswanathan, "An Aerodynamic Assessment of Vehicle-Side Wall Interaction using Numerical Simulations," Int. J. Automot. Mech. Eng. **17**(1), **7587-7598** (2020). https://doi.org/10.15282/ijame.17.1.2020.08.0563

[20] H. Viswanathan, "Aerodynamic performance of several passive vortex generator configurations on an Ahmed body subjected to yaw angles," J. Brazilian Soc. Mech. Sci. Eng. **43**(3), **131** (2021). https://doi.org/10.1007/s40430-021-02850-8

[21] R. Höld, A. Brenneis, A. Eberle, V. Schwarz, and R. Siegert, "Numerical simulation of aeroacoustic sound generated by generic bodies placed on a plate: Part I - Prediction of

aeroacoustic sources,"in 5th AIAA/CEAS Aeroacoustics Conf. Exhib. (May), AIAA Paper No. **99-1896** (1999). https://doi.org/10.2514/6.1999-1896.

[22] R. Siegert, V. Schwarz, and J. Reichenberger, "Numerical simulation of aeroacoustic sound generated by generic bodies placed on a plate: Part II - Prediction of radiated sound pressure," 5th AIAA/CEAS Aeroacoustics Conf. Exhib. (May), AIAA Paper No. **99-1895** (1999). https://doi.org/10.2514/6.1999-1896

[23] S. Wang, J.R. Bell, D. Burton, A.H. Herbst, J. Sheridan, and M.C. Thompson, "The performance of different turbulence models (URANS, SAS and DES) for predicting high-speed train slipstream," J. Wind Eng. Ind. Aerodyn. **165**, **46-57** (2017). https://doi.org/10.1016/j.jweia.2017.03.001

[24] J. Ask, and L. Davidson, "A numerical investigation of the flow past a generic side mirror and its impact on sound generation," J. Fluids Eng. Trans. ASME **131**(6), **061102** (2009). https://doi.org/10.1115/1.3129122

[25] J. Ask, and L. Davidson, "The sub-critical flow past a generic side mirror and its impact on sound generation and propagation," Collect. Tech. Pap. - 12th AIAA/CEAS Aeroacoustics Conf. **3**(May), AIAA Paper No. **2006-2558** (2006). https://doi.org/10.2514/6.2006-2558

[26] N. Ashton, and A. Revell, "Key factors in the use of DDES for the flow around a simplified car," Int. J. Heat Fluid Flow **54**, **236-249** (2015). https://doi.org/10.1016/j.ijheatfluidflow.2015.06.002

[27] E. Guilmineau, G.B. Deng, P. Queutey, M. Visonneau, N. Ashton, A. West, S. Lardeau, and A. Revell, "Assessment of RANS and DES methods for realistic automotive models," Comput. Fluids **128**, **1-15** (2016). https://doi.org/10.1016/j.compfluid.2016.01.008

[28] P. Ekman, D. Wieser, T. Virdung, and M. Karlsson, "Assessment of hybrid RANS-LES methods for accurate automotive aerodynamic simulations," J. Wind Eng. Ind. Aerodyn. **206**, **104301** (2020). https://doi.org/10.1016/j.jweia.2020.104301

[29] X. Chen, and M. Li, "Delayed Detached Eddy Simulation of Subcritical Flow past Generic Side Mirror," J. Shanghai Jiaotong Univ. **24**(1), **107-112** (2019). https://doi.org/10.1007/s12204-019-2044-z

[30] F. Menter, "Stress-blended eddy simulation (SBES)—A new paradigm in hybrid RANS-LES modeling," Notes Numer. Fluid Mech. Multidiscip. Des. **137**, **27-37** (2018).

https://doi.org/10.1007/978-3-319-70031-13

[31] F. Menter, A. Hüppe, A. Matyushenko, and D. Kolmogorov, "An overview of hybrid rans–les models developed for industrial cfd," Appl. Sci. **11**(6), **2459** (2021). https://doi.org/10.3390/app11062459

[32] B.C. Kim, and K. Chang, "Assessment of hybrid RANS/LES models in heat and fluid flows around staggered pin-fin arrays," Energies **13**(14), **3752** (2020). https://doi.org/10.3390/en13143752

[33] K.K. Chode, H. Viswanathan, and K. Chow, "Numerical investigation on the salient features of flow over standard notchback configurations using scale resolving simulations," Comput. Fluids **210**, **104666** (2020). https://doi.org/10.1016/j.compfluid.2020.104666

[34] A.H. Dawi, and R.A.D. Akkermans, "Direct noise computation of a generic vehicle model using a finite volume method," Comput. Fluids **191**, **104243** (2019). https://doi.org/10.1016/j.compfluid.2019.104243

[35] M. Islam, F. Decker, M. Hartmann, A. Jaeger, T. Lemke, J. Ocker, V. Schwarz, F. Ullrich, B. Crouse, G. Balasubramanian, and F. Mendonca, "Investigations of Sunroof Buffeting in an Idealised Generic Vehicle Model - Part II: Numerical Simulations," 14th AIAA/CEAS Aeroacoustics Conf. (29th AIAA Aeroacoustics Conf. (May), AIAA Paper No. **2008-2901** (2008). https://doi.org/10.2514/6.2008-2901

[36] D. Evans, M. Hartmann, and J. Delfs, "Beamforming for point force surface sources in numerical data," J. Sound Vib. **458**, **303-319** (2019). https://doi.org/10.1016/j.jsv.2019.05.030

[37] S. Müller, S. Becker, C. Gabriel, R. Lerch, and F. Ullrich, "Flow-induced input of sound to the interior of a simplified car model depending on various setup parameters," 19th AIAA/CEAS Aeroacoustics Conf., **28** AIAA Paper No. **2013-2029** (2013). https://doi.org/10.2514/6.2013-2029

[38] M.A. Alhawwary, and Z.J. Wang, "Implementation of a fwh approach in a high-order les tool for aeroacoustic noise predictions," AIAA Scitech 2020 Forum **1 PartF**(January),AIAA Paper No. **2020-1724** (2020). https://doi.org/10.2514/6.2020-1724

[39] Y. Wang, Z. Hu, and D. Thompson, "Numerical investigations on the flow over cubes with rounded corners and the noise emitted," Comput. Fluids, **104521** (2020). https://doi.org/10.1016/j.compfluid.2020.104521

[40] T.A. Smith, and C.A. Klettner, "Airfoil trailing-edge noise and drag reduction at a moderate Reynolds number using wavy geometries," Phys. Fluids **34**(11), **117107** (2022). https://doi.org/10.1063/5.0120124

[41] W.C.P. Van Der Velden, A.H. Van Zuijlen, and D. Ragni, "Flow topology and noise emission around straight, serrated and slitted trailing edges using the lattice Boltzmann methodology," 22nd AIAA/CEAS Aeroacoustics Conf. 2016 (May), AIAA Paper No. **2016-3021** (2016). https://doi.org/10.2514/6.2016-3021

[42] J. Ye, M. Xu, P. Xing, Y. Cheng, D. Meng, Y. Tang, and M. Zhu, "Investigation of aerodynamic noise reduction of exterior side view mirror based on bionic shark fin structure," Appl. Acoust. **182**, **108188** (2021). https://doi.org/10.1016/j.apacoust.2021.108188

[43] C. Zheng, P. Zhou, S. Zhong, and X. Zhang, "On the cylinder noise and drag reductions in different Reynolds number ranges using surface pattern fabrics," Phys. Fluids **35**(3), **035111** (2023). https://doi.org/10.1063/5.0138074

[44] A. Celik, L. Bowen, and M. Azarpeyvand, "Experimental investigation on the unsteady surface pressure fluctuation patterns over an airfoil," Phys. Fluids **34**(10), **105134** (2022). https://doi.org/10.1063/5.0114764

[45] G. Chen, B. Zang, and M. Azarpeyvand, "Numerical investigation on aerodynamic noise of flow past a cylinder with different spanwise lengths," Phys. Fluids **35**(3), **035128** (2023). https://doi.org/10.1063/5.0139731

[46] X. Ji, L. Wang, S. Ravi, F.B. Tian, J. Young, and J.C.S. Lai, "Influences of serrated trailing edge on the aerodynamic and aeroacoustic performance of a flapping wing during hovering flight," Phys. Fluids **34**(1), **011902** (2022). https://doi.org/10.1063/5.0070450

[47] K. Nusser, "Investigation of the Fluid-Structure-Acoustics Interaction on a Simplified Car Model," Ph.D. Thesis (Friedrich-Alexander University Erlangen-Nürnberg, 2019).

[48] S.G. Cai, S. Mozaffari, J. Jacob, and P. Sagaut, "Application of immersed boundary based turbulence wall modeling to the Ahmed body aerodynamics," Phys. Fluids **34**(9), **095106** (2022). https://doi.org/10.1063/5.0098232

[49] C. Lai, S. Zhu, S. Feng, G. Zhai, L. Tan, and S. Obayashi, "Flow characteristics and wake topology of two-seat convertibles," Phys. Fluids **35**(1), **015144** (2023). https://doi.org/10.1063/5.0134090

[50] J. Cho, T.-K. Kim, K.-H. Kim, and K. Yee, "Comparative investigation on the aerodynamic effects of combined use of underbody drag reduction devices applied to real sedan," Int. J. Automot. Technol. **18**(6), **959-971** (2017). https://doi.org/10.1007/s12239-017-0094-5

[51] W.-H. Hucho, *Aerodynamics of Road Vehicles : From Fluid Mechanics to Vehicle Engineering* (Society of Automotive Engineers, Warrendale, PA, 1998).

[52] M. Rouméas, P. Gilliéron, and A. Kourta, "Analysis and control of the near-wake flow over a square-back geometry," Comput. Fluids **38**(1), **60-70** (2009). https://doi.org/10.1016/j.compfluid.2008.01.009

[53] G. Pavia, "Characterisation of the Unsteady Wake of a Square-Back Road Vehicle," Ph.D. thesis (Loughborough University, 2019).

[54] G. Bonnavion, O. Cadot, V. Herbert, S. Parpais, R. Vigneron, and J. Délery, "Asymmetry and global instability of real minivans' wake," J. Wind Eng. Ind. Aerodyn. **184**(November 2018), **77–89** (2019). https://doi.org/10.1016/j.jweia.2018.11.006

[55] A. Tosh, M. Caraeni, and D. Caraeni, "A hybrid computational aeroacoustic method for low speed flows," 2018 AIAA/CEAS Aeroacoustics Conf., AIAA Paper No. **2018-4096** (2018). https://doi.org/10.2514/6.2018-4096

[56] J. Ask, and L. Davidson, "Flow and dipole source evaluation of a generic SUV," J. Fluids Eng. Trans. ASME **132**(5), **0511111** (2010). https://doi.org/10.1115/1.4001340

[57] K. Nusser, S. Müller, C. Scheit, M. Oswald, and S. Becker, in *ERCOFTAC Ser.*, edited by D.G.E. Grigoriadis, B.J. Geurts, H. Kuerten, J. Fröhlich, and V. Armenio (Springer International Publishing, Cham, 2018), **24**, 243–249 (2018). https://doi.org/10.1007/978-3-319-63212-4_30